Fe(III) Loaded Chitosan-Biochar Composite Fibers for the Removal of Phosphate from Water

Kumuduni Niroshika Palansooriya[a,1], Sok Kim[b,1], Avanthi Deshani Igalavithana[a,c], Yohey Hashimoto[d], Yoon-E Choi[b], Raj Mukhopadhyay[e], Binoy Sarkar[f], Yong Sik Ok[a,*]

[a] *Korea Biochar Research Center, APRU Sustainable Waste Management Program & Division of Environmental Science and Ecological Engineering, Korea University, Seoul 02841, South Korea*

[b] *Division of Environmental Science and Ecological Engineering, Korea University, Seoul 02841, Republic of Korea*

[c] *Department of Soil Science, University of Peradeniya 20400, Sri Lanka*

[d] *Department of Bioapplications and Systems Engineering, Tokyo University of Agriculture and Technology, Tokyo 184-8588, Japan*

[e] *Division of Irrigation and Drainage Engineering, ICAR-Central Soil Salinity Research Institute, Haryana, India*

[f] *Lancaster Environment Centre, Lancaster University, Lancaster LA1 4YQ, United Kingdom*

*Corresponding author:

Prof. Yong Sik Ok, Korea University. E-mail: yongsikok@korea.ac.kr. Tel: +82-2-3290-3044

[1] These authors share co-first authorship.

Highlights

- Chitosan-biochar composite fibers (FBC) were prepared from paper mill sludge.
- FBCs showed higher phosphate removal efficiency compared to biochars.
- Phosphate adsorption isotherm of FBCs fitted to Redlich–Peterson model.
- Phosphate adsorption was governed mainly via chemisorption.
- XANES spectra confirmed phosphate association with Fe minerals (Fe-P) on FBCs.

Graphical abstract

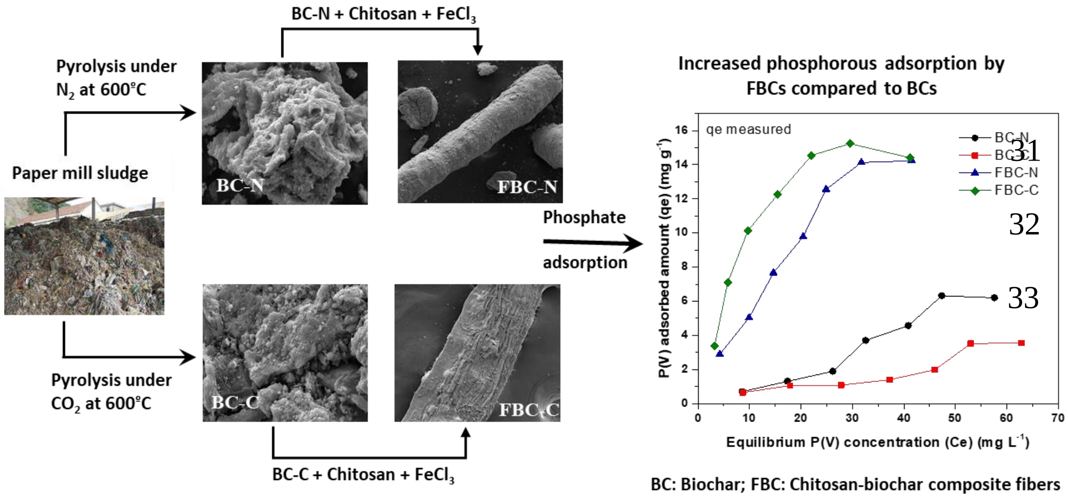

Abstract

Excess phosphorous (P) in aquatic systems causes adverse environmental impacts including eutrophication. This study fabricated Fe(III) loaded chitosan-biochar composite fibers (FBC-N and FBC-C) from paper mill sludge biochar produced under N_2 (BC-N) and CO_2 (BC-C) conditions at 600 °C for adsorptive removal of phosphate from water. Investigations using SEM/EDX, XPS, Raman spectroscopy, and specific surface area measurement revealed the morphological and physico-chemical characteristics of the FBC. The Freundlich isotherm model well described the phosphate adsorption on BC-N, while the Redlich–Peterson model best fitted to data of three other adsorbents. The maximum adsorption capacities were 9.63, 8.56, 16.43, and 19.24 mg P g^{-1} for BC-N, BC-C, FBC-N, and FBC-C, respectively, indicating better adsorption by Fe(III) loaded chitosan-biochar composite fibers (FBCs) than pristine biochars. The pseudo-first-order kinetic model suitably explained the phosphate adsorption on BC-C and BC-N, while data of FBC-N and FBC-C followed the pseudo-second-order and Elovich model, respectively. Molecular level observations of the P K-edge XANES spectra confirmed that phosphate associated with iron (Fe) minerals (Fe-P) were the primary species in all the adsorbents. This study suggests that FBCs hold high potential as inexpensive and green adsorbents for remediating phosphate in contaminated water, and encourage resource recovery via bio-based management of hazardous waste.

Keywords: *Eutrophication; Clean water and sanitation; Charcoal; Water quality; Chitosan; XANES*

1. Introduction

For several decades, water polluted with inorganic/organic pollutants has been perceived as a significant threat as it causes acute/chronic health risks to all living creatures (Geng et al., 2019; Palansooriya et al., 2019b). Phosphorus is an essential nutrient element for all organisms and is vital for the functioning of ecosystems (Huang et al., 2020a). In aqueous phase, phosphoric acid (H_3PO_4) is dissociated at different pKa values to produce phosphate species ($H_2PO_4^-$ at pK_a=2.15; HPO_4^{2-} at pKa=7.20, and PO_4^{3-} at pKa=12.35). Thus, the total phosphate is the sum of all these anionic phosphate species (Awual, 2019). However, when the excess P that is not assimilated in the biogeochemical P cycle, it is released into the waters and causes eutrophication (Hautier et al., 2020). Eutrophication leads to production of toxic algal blooms, loss of biodiversity, and dead zones in aquatic ecosystems (Yang et al., 2019). Therefore, effective and practical measures for phosphate removal from water bodies is of great importance.

Numerous physicochemical and biochemical treatments, including membrane filtration (Yang et al., 2014), reverse osmosis (Luo et al., 2016), electro-dialysis (Zhang et al., 2013), electrocoagulation (İrdemez et al., 2006), ion exchange (Acelas et al., 2015), chemical precipitation (Lei et al., 2019), adsorption (Xiong et al., 2017), and microbial processes (Delgadillo-Mirquez et al., 2016) have been developed for the removal of phosphate from water. Adsorption has gained considerable attention because of its ease operation, cost effectiveness, and design flexibility. Various phosphate adsorbents, including carbon-based materials (e.g., biochar and activated carbon) (Khalil et al., 2017), iron-based adsorbents (e.g., zero valent iron, Fe–Cu binary oxides, Fe–Zr binary oxide) (Li et al., 2014; Ren et al., 2012; Wen et al., 2014), zeolites (Goscianska et al., 2018), synthetic polymers (e.g., polyvinyl alcohol) (Ding et al., 2018), and agro-wastes (e.g., rice husk) (Mor et al., 2016) have been used for phosphate removal from water. Many of these adsorbents exhibit technical drawbacks in terms of low adsorption capacity, small particle sizes that are difficult to handle, challenges in post-application separation and collection, poor chemical and mechanical stability in aqueous media, and high cost, (Blaney et al., 2007; Emmanuelawati et al., 2013) which greatly impede their practical implementation for phosphate removal from wastewater. Hence, there is a need to develop inexpensive, reliable, and sustainable adsorbents for phosphate removal from aqueous solutions by solving the observed technical constraints while achieving P recovery for enhancing food production.

Chitosan is a ubiquitous, biodegradable, and nontoxic biopolymer obtained from shrimp and other crustacean organisms (Luo et al., 2020). As it is rich in amino and hydroxyl functional groups, it can be widely employed in removing ionic metal contaminants (Elwakeel et al., 2021; Li et al., 2018). However, poor chemical/mechanical stability (e.g., poor acidic-resistance) of chitosan limits its practical application for water purification (Osifo et al., 2008). To circumvent this issue of stability, a combination of chitosan and inorganic/organic materials has been identified as a promising technique to improve the chemical and mechanical properties of the polymer. Biochar (Afzal et al., 2018), clay minerals (Rusmin et al., 2015), zeolites (Khanday et al., 2017), fly ash (Sheng et al., 2016), hydroxyapatite (Fan et al., 2019), silica (hybrid functionalized chitosan- Al_2O_3-SiO_2composite) (Zhang et al., 2018b), and TiO_2 (Neghi et al., 2019) and metals (chitosan–metal complex) (Rashid et al., 2018) are some of the inorganic/organic materials that are incorporated with chitosan to fabricate the composites. Moreover, the incorporation of inorganic additive materials in chitosan has shown an increased efficiency of contaminant removal from aqueous systems (Jiang et al., 2013).

Biochar is a carbon-rich material that is obtained from the thermochemical conversion of biomass under oxygen-free/limited conditions (Palansooriya et al., 2019a). It is a green adsorbent that is well-known for the removal of a variety of organic/inorganic contaminants in water (Palansooriya et al., 2019b). However, depending on the type of feedstock and pyrolysis conditions (e.g., temperature and gas environment), the adsorption capacity of biochar can significantly vary (El-Naggar et al., 2019; Herath et al., 2020). Specifically, most biochar products exhibit poor adsorption capacity for anionic contaminants, such as phosphate (Lou et al., 2016; Zhang et al., 2020), arsenic, and nitrite (Tan et al., 2020) due to repulsion forces between biochar surfaces and phosphate ions. Thus, it is imperative to impart desired functionalities to pristine biochar by means of modification to enhance the phosphate removal capability.

Paper mill sludge (PMS), which is a waste from the paper industry, can be used as feedstock for biochar production. PMS contains inorganic Fe and Ca species derived from $FeSO_4$ and $CaCO_3$, which are used during the production of pulp (Cho et al., 2017b; Hu et al., 2015). The high inorganic content in PMS is likely to impart the desired properties to biochar, resulting in an increased adsorption capacity for anionic contaminants, such as phosphate (Cho et al., 2017a). However, the powdery form of biochar is difficult to separate/collect from aqueous phases following phosphate adsorption; therefore, it is less suitable for dynamic adsorption applications. Thus, the conversion of powdery biochar to a form that is easily separable from water following adsorption application can be beneficial for its practical applications.

Incorporation of chitosan with PMS biochar provides a win-win strategy for producing novel chitosan-biochar composite fibers, which can further enhance phosphate adsorption capacity owing to the improved chemical/mechanical stability, surface functional groups, and active sites. In addition, utilization of these wastes (PMS and chitosan) as a resource (waste as raw materials to new products) for sustainable waste management coincide with shifting the current linear model to a circular based economy. Furthermore, waste materials are used to clean water sources while achieving resource recovery. Considering the existing research gaps in the utilization of waste materials (i.e., PMS and chitosan) in phosphate removal (convincing synthesis method and impact of field relevant variable conditions (e.g., pH)), two PMS biochars and two FBCs were fabricated to evaluate their adsorption performances of phosphate under various conditions. The objectives of this study were to: (1) produce biochars from PMS and to fabricate FBCs from PMS biochars; (2) characterize biochars and FBCs using scanning electron microscopy (SEM), X-ray photoelectron spectroscopy (XPS), and specific surface area (SSA) measurements; (3) examine the adsorption isotherms and kinetics to describe the possible interactions between biochars/FBCs and phosphate; and (4) determine the retention characteristics and mechanisms of phosphate on biochars and FBCs using X-ray absorption near edge structure spectroscopy.

2. Materials and methods

2.1. Materials

Chitosan (low molecular weight, deacetylated chitin (75%–85% of deacetylation degree), iron(III) chloride hexahydrate ($FeCl_3{\cdot}6H_2O$, 97%)), and potassium dihydrogen phosphate (KH_2PO_4, 99.5%) were purchased from Sigma-Aldrich (Seoul, Korea). All reagents were prepared in deionized water. Phosphate stock solutions were prepared by dissolving KH_2PO_4 in deionized water. The PMS was obtained from a local paper processing plant (Moorim Paper Co.) in South Korea. N_2 and CO_2 gases used in the production of biochar were ultrahigh purity grades obtained from Daesung Gas Co. (South Korea).

2.2. Preparation of biochar and Fe(III) loaded chitosan-biochar composite fibers

Two types of biochars were produced from the PMS. The detailed procedure of biochar production was described by (Cho et al., 2017b). Briefly, the PMS was first oven-dried at 60 °C for 2-days, crushed, and pyrolyzed at 600 °C at a heating rate of 15 °C min^{-1} under CO_2 and N_2 environments using a quartz tubular reactor (CGQ-0900T-13, Chemglass; 25.4 mm outer diameter and 0.6 m length). The produced biochars were named as BC-N (under N_2 environment) and BC-C (under CO_2 environment). To fabricate FBC, 4% (w/w) chitosan solution was prepared in a 5% (v/v) acetic acid solution. The prepared chitosan solution (115 g) was mixed with 3.22 g of respective biochar (<75 μm). Simultaneously, 10 g of $FeCl_3 \cdot 6H_2O$ was added to each chitosan/biochar suspension with vigorous agitation. Then, the mixture was extruded through a 0.2-mm diameter plastic hub needle (TAEHA Co., Namyangju, Korea) into a 2 *M* NaOH solution (~14 pH) for chitosan gelation. The FBC was cross-linked in a glutaraldehyde solution (0.6 mL/L) at 25 °C for 2 h. After the cross-linking reaction, the FBC was rinsed with deionized water several times until it attained a neutral pH, after which it was lyophilized. The FBCs thus produced with BC-N and BC-C were named FBC-N and FBC-C, respectively.

2.3. Characterization of biochar and Fe(III) loaded chitosan-biochar composite fibers

The surface morphology and elemental composition of biochar and FBC were determined using a field-emission scanning electron microscope (FE-SEM; Quanta 250 FEG) equipped with an energy dispersive spectrometer (SEM-EDS). The SSA, pore volume, pore size, and porosity were determined by the Brunauer–Emmett–Teller (BET) method with a volumetric adsorption analyzer (ASAP 2020, Micrometrics) using N_2 adsorption–desorption isotherm analyses at -

196 °C. Characteristics related to the functional groups of the materials were assessed by determining the changes in the selected elemental signals (C1s and N1s) using XPS. Spectra were collected on a monochromatic Al Kα (1486.7 eV) X-ray source at 40 eV pass energy. Furthermore, the structural properties of carbon in the samples were characterized using a Raman spectrophotometer (LabRam ARAMIS IR2, Horiba Jobin Yvon). The crystallographic structures in the samples were identified by X-ray diffraction (XRD) analysis using Cu K α (k = 1.54 °A) radiation at 45 kV within a 2ϴ range of 278–410 (Rigaku, SmartLab).

2.4. Adsorption experiments

Batch experiments were performed in 50 mL polypropylene tubes to assess the phosphate adsorption as affected by initial phosphate concentration, contact time, adsorbent dosage, and solution pH. The four adsorbents were examined for phosphate sorption ability under different conditions. The suspensions were then filtered through a 0.45 μm membrane (syringe) filter; the residual aqueous P concentration was determined by the ascorbic acid method using a UV-VIS spectrophotometer (Genesys 10S UV-VIS, Thermo Fisher Scientific Solutions LLC). All the experiments were performed at room temperature (25 °C) in triplicate.

2.4.1. Adsorption isotherm

Biochar or FBC of 2 g L^{-1} (0.05 g of solid in 25 mL of solution) was mixed with the phosphate solution at 10, 20, 40, 50, 60, and 70 mg P L^{-1} at pH 4. All the vials were sealed and shaken at 120 rpm on a horizontal shaker for 24 h until the apparent equilibrium (see Fig. 6) was reached. At equilibrium, the samples were filtered, and the residual P concentrations were determined. The equilibrium adsorption capacity was calculated using Eq. 1:

$$q_e = [(C_o - C_e) \times V]/M \quad \text{(Eq. 1)}$$

where, q_e is the phosphate adsorption capacity at equilibrium (mg P g^{-1}); C_o and C_e are the initial and equilibrium phosphate concentrations (mg P L^{-1}), respectively; V is the volume of the solution (L); and M is the mass of adsorbent (g).

Different adsorption isotherm models, namely Freundlich, Langmuir, Sips, and Redlich–Peterson (Supplementary Information (SI)) were adopted to fit the experimental data.

2.4.2. Adsorption kinetics

The kinetic tests were conducted using 2 g L^{-1} of adsorbent dosage at pH 4 with 40 mg P L^{-1} of initial phosphate concentration over 24 h. At predetermined time intervals, 1 mL of the suspension was removed from the solution to analyze the P concentration. The phosphate adsorption kinetics data were described by the pseudo-first-order (PFO), pseudo-second-order (PSO), intra-particle diffusion, and Elovich models (SI).

2.4.3. Effect of pH and adsorbent dosage on phosphate adsorption

The influence of adsorbent dosage on phosphate adsorption was determined at 1, 2, and 4 g L^{-1} of adsorbent dosages, at pH 4, and an initial phosphate concentration of 40 mg P L^{-1}. The effect of solution pH was assessed at pH values varying between 2 and 10, initial phosphate concentration of 40 P mg L^{-1}, and adsorbent dosage of 4 g L^{-1}. Experiments were carried out for 24 h. Herein, the adsorption efficiency of each adsorbent was calculated using Eq. 2:

$$\text{Removal efficiency (\%)} = [(C_o - C_e)/C_o] \times 100 \quad \text{(Eq. 2)}$$

2.5. Phosphorus K-edge XANES spectroscopy

Phosphorus K-edge XANES measurements were conducted at Aichi Synchrotron Radiation Center (Aichi, Japan) using a beamline BL6N1 equipped with an InSb (111) monochromator at ambient temperature under a He atmosphere. The XANES spectra of the samples were collected in fluorescence yield mode. The monochromator was calibrated at the whiteline (2481.7 eV) of K_2SO_4's S K-edge X-ray absorption fine structure (XAFS) spectrum. The background and baseline of all spectra were corrected and normalized using the Athena software (Ravel & Newville, 2005). Moreover, linear combination fitting (LCF) of the XANES spectra was performed using all possible binary and ternary combinations of the available P reference compounds measured in previous studies (Yamamoto & Hashimoto, 2017; Yamamoto et al., 2018). The reference compounds used for LCF were hydroxyapatite and tricalcium phosphate for P associated with Ca minerals, strengite, phosphate adsorbed on ferrihydrite for P associated with Fe minerals, and variscite and phosphate adsorbed on gibbsite for P associated with Al minerals. Methods for the preparation of reference samples have been reported in a previous research (Yamamoto & Hashimoto, 2017). The quality of LCF results was quantified through a residual (R) value, after which the top three or four results were reported (SI). The LCF was performed in the relative energy range between -5 and 20 eV.

2.6. Statistical analysis

The adsorption data were presented as mean ± standard error. The kinetic and isotherm adsorption models were fitted by non-linear regression using least square method.

3. Results and discussion

3.1. Surface morphology and elemental composition of adsorbents

The SSA of BC-N (50.58 cm^2 g^{-1}) was greater than that of BC-C (46.02 cm^2 g^{-1}) (Table 1). After producing fibers, the SSA of the FBCs was lower than the original biochars (FBC-N: 7.30 cm^2 g^{-1}; FBC-C; 12.30 cm^2 g^{-1}; Table 1). The pore volume, pore size, and porosity of the biochars and FBCs exhibited a similar trend, showing relatively higher values for biochars than FBCs (Table 1). These observations could be attributed to the blockage of biochar pores by chitosan during fiber preparation (Cui et al., 2016; Zhang et al., 2015). The results were further confirmed by SEM morphology (Fig. S1 and Fig. S2) of biochars and FBCs, where the pore surfaces of FBCs were observed to be covered and encapsulated.

Both biochars had heterogeneous surfaces with highly porous surfaces (Fig. S1), which could have caused high porosity and SSA of the biochars (Table 1). The atomic percentages of elements, namely Mg, Al, Ca, and Fe, that are expected to aid phosphate immobilization, were higher in BC-C than in BC-N (Fig. S1). A high percentage of inorganic elements in the biochars could have resulted from the feedstock (PMS) rich in those elements. For example, $CaCO_3$ and $FeSO_4$ are added during the treatment of papermill wastewater, which ultimately produces PMS rich with Ca and Fe species (Yoon et al., 2017). The surface morphology and elemental composition of FBCs (Fig. S2) were found to be quite different from those of the biochars. FBC-N had a rough surface topography, whereas FBC-C had a wrinkled surface (Fig. S2). The wrinkled surface on FBC-C might be the reason for the higher surface area of FBC-C than that of FBC-N (Table 1), leading to increased phosphate adsorption sites.

3.2. Surface functional groups of adsorbents

Figure 1 shows the high-resolution C1s photoelectron spectra and their deconvolution results for the two biochars along with their corresponding FBCs. For BC-N, four different peaks were observed at 284.6, 285.7, 289.2, and 290.1 eV, which attributed to C atoms in the form of C-H/C, C=C (61.7%), C-OH/C-Cl (30.3%), HO-C=O (5.0%), and carbonates (3.0%), respectively (Araujo et al., 2014; Zhang & Zhang, 2010), with C-H/C, C=C having the most dominant peak. Similar peaks were observed for BC-C at different percentages; however, two new peaks were observed at 283.1 and 286.6 eV, which corresponded to C-metal (8.1%) and C-O-C/C-O (15.4%), respectively (Huang et al., 2016; Zhang & Zhang, 2010). Moreover, the C-OH/C-Cl peak was absent in the case of BC-C. Lee et al. (2017) obtained a similar result, wherein biochar produced from red pepper stalk under N_2 environment showed -OH groups on the surface but did not show -OH group on the surface for biochar produced in a CO_2 environment. This could be due to the interaction between CO_2 and the base functional groups on the biochar surfaces (Lee et al., 2017). In the case of FBC-N, five different peaks were observed at 284.4, 286.1, 287.5, 288.1, and 289.2 eV (Fig. 1), which corresponded to C-H/C, C=C (47.1%), C-O-C, C-O (31.9%), C=N, N-C=O (3.8%), C=O (2.3%), and HO-C=O (14.8%), respectively (Araujo et al., 2014; Zhang & Zhang, 2010). For FBC-C, similar peaks were observed, except C=O. However, a new peak appeared at 282.8 eV, corresponding to C-metal (8.8%), and this represented carbon combined with metallic elements. The formation of organometallic Ca_2C and/or Fe_3C was likely triggered by the addition of $FeCl_3$ or Ca and Fe metals that were inherently present in PMS (Ghods et al., 2011). The C-metal peak did not appear in either the FBC-N or BC-N C1s spectra (Fig. 1). A previous study reported that biochar produced under a CO_2 environment contained more aromatic carbon structures than that produced under an N_2 environment (Igalavithana et al., 2019). Aromatic carbon structures can increase the biochar surface negativity, thereby increasing the stabilization of metals on biochar surfaces (Igalavithana et al., 2019). Similarly, Ca and Fe present in PMS were well-stabilized during the production of BC-C and were successfully embedded in FBC-C. Compared to biochars, FBCs had new N-containing peaks corresponding to C=N (62.4% in FBC-N) and N-C=O (5.6% in FBC-N and 65.9% in FBC-C). This could be due to the addition of N from chitosan during FBC preparation (Zhang et al., 2018a).

High-resolution N1s spectra and their deconvolution results for BC-N, BC-C, FBC-N, and FBC-C are presented in Fig. 2. Two dominant peaks, namely C–N and N–C =O were observed in both the biochars. BC-N had a lower proportion of N-C=O (23.2%) than BC-C (N-C=O: 46.4%). However, proportions of C-N were comparable in BC-N (44.3%) and BC-C (46.0%). In BC-N, a peak centered at 403.9 eV represented the CH_3CO-NH group(Zhang & Zhang, 2010) which was absent in BC-C. Moreover, the C-NH_2 group was observed in both the biochars; however, BC-N (25.9%) had a higher proportion of C-NH_2 than BC-C (3.8%). Due to the acidic nature of CO_2, alkaline amines (-NH_2) could be neutralized by reacting with CO_2 (Vaidya & Kenig, 2007), thereby eliminating -NH_2 groups from biochar surfaces. This was the plausible reason for the disappearance of CH_3CO-NH from BC-C and the higher proportion of C-NH_2 groups on BC-N than BC-C. In the FBC-N spectra, four different peaks centered at 397.7 (–NH_2), 399.1 (C=N), 399.9 (N-C=O), and 400.1 eV (C-NH_2) were observed (Fig. 2). In FBC-C, four peaks were centered at 397.2 (metal nitrides), 398.4 (C–N), 399.6 (N–C =O), and 403.5 eV (CH_3CO-NH) (Fig. 2). In FBC-N and FBC-C, the dominant peaks were C=N (62.4%) and N-C=O (65.9%), respectively. Therefore, following the preparation of fibers, FCB-N was functionalized with C=N and -NH_2 groups, whereas FBC-C was functionalized with the CH_3CO-NH group. These groups were not present in the corresponding biochar. The difference in the Cs1 and N1s spectra between biochar and FBCs originates from the modification of pristine biochars with $FeCl_3$ and chitosan, respectively, as also observed by Zhang et al. (2015). The XPS results further indicated that FBCs were fabricated successfully in this study.

3.3. *Raman spectroscopy*

The aromaticity and aliphaticity of the adsorbents were examined by Raman spectroscopic analysis (Fig. 3). The deconvoluted Raman spectra of all four adsorbents revealed a D band between 1350 and 1372 cm^{-1}, which represented large aromatic ring systems containing six or more rings (Yang et al., 2018b). The G band, between 1599 and 1601 cm^{-1}, represented the sp^2-bonded graphite crystallite and alkene C=C (Li et al., 2006b). Another major band (G_L) was observed between the D and G bands in all four adsorbents, which represented aromatics with 3–5 rings and amorphous carbon structures (Li et al., 2006b). Peak assignments for all characteristic subpeaks are listed in Table S1. The ratio of integrated intensity (peak area (A)) between the D and G bands (A_D/A_G) is an important measure to study the degree of aromaticity and crystalline or graphite-like carbon structures (Igalavithana et al., 2018; Li et al., 2006a). A lower A_D/A_G ratio implies more ordered carbon structures or a higher degree of graphitization of biochar (Wei et al., 2016). The A_D/A_G ratios of BC-N, BC-C, FBC-N, and FBC-C are presented in Table S2. BC-N (1.93) and FBC-N (1.50) had lower A_D/A_G ratios than BC-C (3.16) and FBC-C (2.54), indicating the effect of biochar production atmosphere (CO_2 and N_2) on their properties. Biochar produced under a CO_2 environment showed defective carbon structures due to the reaction of volatile organic matter of PMS with CO_2, which did not occur in the case of an N_2 environment (Cho et al., 2016). This could explain the higher A_D/A_G ratios in adsorbents derived in a CO_2 environment than in an N_2 environment. However, the production of FBCs led to a decrease in the A_D/A_G ratio compared to their corresponding biochars (Table S2). The A_D/A_G ratio decreased from 1.93 in the case of BC-N to 1.50 with respect to FBC-N, whereas that of BC-C decreased from 3.16 to 2.54 for FBC-C. These results indicated that the production of

FBCs tended to have more well-ordered carbon structures in the fabricated materials. The S band represents $C_{aromatic}$–C_{alkyl}, aromatic (aliphatic) ethers, C–C on hydroaromatic rings, hexagonal diamond carbon sp^3, and C–H on aromatic rings(Li et al., 2006b). The ratio of A_S/A_G could give an idea about the O-containing functional groups, or decarbonization and decarboxylation reactions in the materials (Yang et al., 2018b). S bands were observed in BC-C and FBC-C, but not in BC-N and FBC-N (Fig. 3). Moreover, a high A_S/A_G ratio of BC-C (Table S2) implied that BC-C underwent decarbonization and decarboxylation reactions and lost its O-containing functional groups during biochar production (Li et al., 2006a; Yang et al., 2018a). The A_S/A_G ratio also decreased in FBC-C following the fabrication of BC-C with $FeCl_3$ and chitosan (Table S2).

3.4. Phosphate adsorption

3.4.1. Adsorption isotherms

The amount of phosphate adsorbed at equilibrium phosphate concentration on the four adsorbents followed the order of FBC-C> FBC-N > BC-N> BC-C (Fig. 4). The phosphate adsorption capacities increased with increasing equilibrium concentrations of all four adsorbents. The adsorption isotherm data were fitted to the Freundlich, Langmuir, Sips, and Redlich–Peterson models; the model fitting parameters are listed in Table 2. The non-linear fitting of each model is shown in Figs. S3–S6. BC-N was best fitted to the Freundlich isotherm with higher correlation coefficients ($R^2 = 0.89$) and higher ratio of performance to deviation (RPD = 2.37). The Redlich–Peterson model provided a better fit for the adsorbents, such as BC-C ($R^2 = 0.77$; RPD =1.72), FBC-N ($R^2 = 0.97$; RPD =5.72), and FBC-C ($R^2 = 0.91$; RPD =3.38) with high R^2 and RPD values (Table 2). However, the Redlich–Peterson equation is a combination of

Langmuir and Freundlich equations (Hong et al., 2009; Ng et al., 2002). If the exponent "g" of the Redlich–Peterson equation tends to zero, the equation becomes more Freundlich. In contrast, the equation follows the Langmuir condition when the exponent "g" reaches one (Ng et al., 2002). As the "g" value for BC-C is zero, it is evident that BC-C follows Freundlich adsorption isotherm, whereas FBC-N (g=2.36) and FBC-C (g=1.54) follow Langmuir adsorption isotherms. This suggests that BC-N and BC-C have heterogeneous surface and the phosphate adsorption occurred as multilayer sorption (Jiang et al., 2013). Whereas FBCs have homogeneous surfaces and phosphate was adsorbed as monolayer surface coverage without interaction between the adsorbed phosphate ions (Zhao & Feng, 2016).

The Langmuir maximum phosphate adsorption capacities of BC-C, BC-N, FBC-N, and FBC-C were 9.63, 8.56, 16.43, and 19.24 mg P g^{-1}, respectively (Table 2). The phosphate adsorption capacities of the FBCs were much higher than those of the biochar, confirming that the modification with chitosan and Fe greatly contributed to the adsorption ability of the adsorbents. The FBC-C was found slightly superior to FBC-N for phosphate removal in aqueous system probably due to the availability of more functional groups in FBC-C (Fig. 1 and Fig. 2) which increased the phosphate removal capacity. Moreover, SEM-EDS elemental composition clearly indicated the presence of almost 2 times higher Fe content (weight %) in FBC-C (53.79%) than FBC-N (29.65%) which contributed to better phosphate removal efficiency for FBC-C than FBC-N and other biochars (Fig. S2). Similarly, previous studies have shown that biochar modification with chitosan and metals (e.g., Fe, Mg, Zr, and La) enhanced the phosphate removal efficiency in aqueous solutions (Cui et al., 2016; Cui et al., 2019; Huang et al., 2020b; Liu & Zhang, 2015). Nevertheless, Fe(III)-doped chitosan and crosslinked Fe(III)-chitosan composites exhibited 15.7 and 10.2 mg P g^{-1} of phosphate adsorption capacities, respectively

(Zhang et al., 2018a). Chitosan biocomposites chelated with Ca^{2+} ion showed 13.44 mg g^{-1} of phosphate adsorption capacity (Kumar & Viswanathan, 2017). In comparison to the results in the literature, FBC-C and FBC-N are superior in terms of phosphate removal in aqueous system.

The calculated separation factor (R_L) value refers to the isotherm type that is unfavorable ($R_L > 1$), linear ($R_L = 1$), favorable ($0 < R_L < 1$), or irreversible ($R_L = 0$) (Ahmad et al., 2013). In this study, the R_L values were <1 for FBCs, indicating that phosphate adsorption was favorable; thus, adsorption on FBC-C was the most favorable among all the adsorbents (Fig. 5). However, the R_L values of the biochars were >1, indicating that phosphate adsorption was unfavorable for BC-N and BC-C. Therefore, the fabrication of biochars with $FeCl_3$ and chitosan transformed the unfavorable phosphate adsorption into a favorable process for FBCs. Zhang et al. (2019) found that phosphate adsorption to biochars derived from vegetable wastes was very low. Similarly, Micháleková-Richveisová et al. (2017) observed low phosphate adsorption capacities for biochar derived from corn cobs, garden wood waste, and wood chips (0.036, 0.132, and 0.296 mg g^{-1}, respectively). A Fe-impregnation of biochar was done to improve the phosphate removal efficiency, but the resultant adsorption capacities were also not satisfactory (1.988, 2.754, and 3.201 mg g^{-1}, respectively). These findings indicate the novelty of the current study synthesizing advanced functionalized materials (e.g., FBCs) using biochar to maximize phosphate removal efficiency.

3.4.2. Adsorption kinetics

The phosphate adsorption kinetics were studied in order to determine the factors controlling the rate of adsorption, which might provide profound insight for the adsorption process. The phosphate adsorption process on biochars and FBCs was rapid in the beginning (first 4 h); afterwards, it increased slowly until the plateau of adsorption equilibrium was achieved (Fig. 6). The phosphate adsorption kinetic data were fitted to the PFO, PSO, intra-particle diffusion, and Elovich models. The model fitting parameters are listed in Table 3. The model fittings of the four adsorbents are shown in Figs. S7–S10. The results showed that the PFO model better fitted the experimental data of BC-N (R^2 = 0.91; RPD = 3.41) and BC-C (R^2 = 0.77; RPD = 1.98), suggesting that the adsorption process mainly depends on the equilibrium phosphate concentration in the solution (Mandal & Singh, 2016). In contrast, FBC-N (R^2 = 0.97; RPD =5.40) fitted well to the PSO model, indicating that phosphate adsorption is a chemisorption process, which may involve a chemical reaction between PO_4^{3-} and functional groups on the biochar surfaces (Wang et al., 2018). Moreover, it suggests that the adsorption rate of phosphate is more dependent on the availability of adsorption sites on the surface of FBC-N than the phosphate concentration in the solution (Liu, 2008; Mandal & Singh, 2016). FBC-C showed the best fit with the Elovich model (R^2 = 0.95; RPD = 4.33), which describes the chemical adsorption of phosphate into FBC-C. The Elovich model further explains that the rate of adsorption decreases as surface area coverage increases (Wu et al., 2009).

3.4.3. Effect of solution pH and adsorbent dosage

The initial pH of the solution is a key factor that controls phosphate adsorption. This is because pH affects the molecular form of phosphate in the solution as well as the properties of adsorbents (Aswin Kumar & Viswanathan, 2018). When the solution pH is acidic (between 2–3.5), H_3PO_4 and $H_2PO_4^-$ are the dominant species of phosphate. In contrast, when the pH is basic (between 9–11), HPO_4^{2-} is the dominant species (Cui et al., 2016). Thus, the changes in solution pH can largely affect the phosphate removal efficiency of an adsorbent by influencing phosphate speciation and ionization in the solution (Jang & Lee, 2019). The phosphate removal efficiencies (%) of both biochars were higher at a pH range of 6–10, as compared to a lower pH range (Fig. 7). However, FBCs showed high phosphate removal efficiency in acidic pH, which decreased with increasing pH (Fig. 7). Although FBCs showed the highest phosphate removal efficiency at pH 2, FBCs tended to dissolve under such strongly acidic conditions. However, substantial phosphate removal efficiency was observed at pH 4 for FBC-N (39.8%) and FBC-C (54.7%), whereas the corresponding biochars showed lower removal efficiency at all pH values compared to the FBCs (Fig. 7). Chitosan is rich in amino groups that can be readily protonated, leading to the production of positively charged groups on FBCs under acidic conditions (Chatterjee & Woo, 2009). Thus, greater phosphate adsorption capacity at lower pH might be due to the electrostatic interactions between the phosphate anions and positively charged surface of FBCs, which is similar to the results of previous studies (Bozorgpour et al., 2016; Jiang et al., 2013; Zhang et al., 2018a). Under alkaline conditions, electrostatic repulsion along with increased competition and diffusion resistance results from the elevated hydroxide ions, which leads to the reduction in phosphate removal efficiency in the solutions (Cui et al., 2019).

The phosphate removal efficiencies increased with increasing adsorbent dosage, although the biochars tended to release phosphate at 1 g L^{-1} of adsorbent dosage (Fig. S11). As explained by Zhang et al. (2020), at lower initial phosphate concentrations, biochar tends to release phosphate rather than adsorbing. Hence, the “net adsorption” of phosphate depends on the release of endogenous phosphate from biochar into aqueous system and the adsorption of exogenous phosphate by biochar (Zhang et al., 2020).

The increase in adsorbent dosage from 1 to 4 g L^{-1} for FBC-N and FBC-C increased their phosphate removal efficiencies from 18.6 to 63.6% and 26.6. 80.8%, respectively (Fig. S11). This could be because an increase in the adsorbent dosage could increase the number of active sites in FBCs (Zhao & Feng, 2016).

Overall, pH edge study confirmed that pH ~ 4.0 was the optimum pH for phosphate removal with the highest amount of phosphate removed at this pH level. To maximize the adsorption capabilities in biochars and FBCs, the optimal dosage was selected as 2 g L^{-1}.

3.4.4. Phosphate adsorption mechanisms: Macroscopic observation

Adsorption isotherm and kinetic studies revealed that the adsorption of phosphate on biochars and FBCs was dominated by chemisorption. As confirmed by the adsorption edge study (Fig. 7), electrostatic attraction between the positively charged surfaces of FBCs and phosphate anions was the main mechanism for phosphate adsorption. Natural river waters have considerable Cl^-, NO_3^- and SO_4^{2-} concentrations co-existing with phosphate anions. The selectivity of phosphate adsorption on a hydrophobic adsorbent depends on the Hofmeister series where the adsorbent prefers to adsorb less hydrated anions over highly hydrated anions given the charges of the anions are equal (Awual et al., 2019a). The affinity of monovalent anions to a hydrophobic adsorbent follows the order: $OH^- \sim F^- < H_2PO_4^- < HCO_3^- < Cl^- < HSO_3^- < Br^- < NO_3^- < I^- < ClO_4^-$ (Awual & Jyo, 2009). Dominant phosphate species in solution at pH < 5.0 is $H_2PO_4^-$, whereas those at pH > 5.0 and at pH = 12 become HPO_4^{2-} and PO_4^{3-}, respectively (Awual & Jyo, 2011). In this study, the FBCs were rich in amine ($-NH_2$) and hydroxyl (–OH) functional groups (Fig. 1 and Fig. 2) due to the incorporation of chitosan. The amine and hydroxyl groups bonded with $H_2PO_4^-$ and HPO_4^{2-} though H^+ ion transfer from the parent acid (H_3PO_4) (Eqs. 3, 4, 5 and 6). In addition, the $-NH_2$ and –OH groups were subjected to protonation under acidic conditions, leading to the formation of positively charged sites, thereby enabling the adsorption of $H_2PO_4^-$ and HPO_4^{2-} through electrostatic attraction at low pH (~4.0) (Fig. 7) (Awual et al., 2019b; Awual et al., 2015; Cui et al., 2019). However, at high pH (> 5.0), the hydrophobic BC-C and BC-N adsorbed relatively greater amounts of phosphate (HPO_4^{2-} species in particular) through strong H-bond complexation than at low pH. This was likely due to the higher basicity of the predominant HPO_4^{2-} species than NO_3^-, Cl^- (released from BC-N and BC-C) or SO_4^{2-} at high pH (Awual & Jyo, 2011) (Fig. 7). Furthermore, ligand exchange between HPO_4^{2-} and –OH or Cl^- on the adsorbent (Awual et al., 2011; Awual et al., 2014) likely occurred because there were significant amounts of –OH and Cl^- on the biochar surfaces (Fig. 1 and Fig. S1). Prevalence of PO_4^{3-} in the current study was unlikely because the system pH seldom crossed 10.0. The mechanistic insights of phosphate adsorption suggested that the novel FBCs hold a great potential for eutrophication management in real water even in the co-existence of competing anions such as NO_3^-, Cl^- and SO_4^{2-}.

H^+ transfer and adsorption:

$\text{FBC-NH}_2 + H^+ + H_2PO_4^- = \text{FBC-NH}_3^+\cdots H_2PO_4^-$ (pH < 5.0) (Eq. 3)

$\text{FBC-NH}_2 + H^+ + HPO_4^{2-} = \text{FBC-NH}_3^+\cdots HPO_4^{2-}$ (pH > 5.0) (Eq. 4)

$\text{FBC-OH} + H^+ + H_2PO_4^- = \text{FBC- OH}_2^+\cdots H_2PO_4^-$ (pH < 5.0) (Eq. 5)

$\text{FBC-OH} + H^+ + HPO_4^{2-} = \text{FBC- OH}_2^+\cdots HPO_4^{2-}$ (pH > 5.0) (Eq. 6)

Moreover, abundant amounts of Mg, Al, Ca, and Fe on the biochar (Fig. S1) and Ca and Fe on FBC surfaces (Fig. S2) could stabilize phosphate via chemical precipitation. For example, Yao et al. (2013) observed the formation of $MgHPO_4$ and $Mg(H_2PO_4)_2$ crystals on Mg-rich biochar in a phosphate adsorption study which suggested that chemical precipitation play an important role in phosphate removal from aqueous solutions.

Overall, the increased adsorption of phosphate on FBCs over biochars was mainly due to the incorporation of chitosan and grafting of $FeCl_3$ in the fabricated adsorbents. The use of chitosan and $FeCl_3$ not only facilitated the stabilization of the biochar, but also significantly enhanced the adsorption capacity of phosphate.

3.4.5. Phosphate adsorption: Molecular observation

Figure 8 shows the P K-edge XANES spectra of the biochar samples together with P reference compounds that yielded the best fits by LCF analysis. All XANES spectra of biochar samples had pre-edge peaks at approximately 2145 eV, indicating the presence of phosphate associated with Fe (Khare et al., 2004). The XANES spectra of all samples were also characterized by the shoulder between 2151 and 2154 eV, indicating the presence of phosphate associated with Ca (Hashimoto et al., 2014). These visual observations of the XANES spectra unambiguously indicated the presence of phosphate species in the samples. Due to their similar XANES spectra, Yamamoto et al. (2018) suggested that it was not ideal to differentiate the phosphate species between adsorbed phases (e.g., phosphate adsorbed on ferrihydrite) and minerals (e.g., strengite). Rather, the LCF results were reported as a group of phosphate species associated with Fe (Fe-P), Ca (Ca-P), and Al (Al-P) (Table S3). In the present study, we used XANES data to determine the phosphate species in the samples, given that the P in the samples was mainly present in an inorganic form (i.e. phosphate forms).

The results of LCF on BC-N demonstrated that phosphate occurred mainly as Fe-P (43%) and Ca-P (34%), and to a lesser extent as Al-P (16%). The BC-C also had similar phosphate species with different proportions (55% of Fe-P, 27% of Ca-P, and 13% of Al-P). In the biochar samples, Fe (39-47%), Ca (8-11%), and Al (1.5%) were the major components of the elements, suggesting that phosphate possibly occurred with these metal cations. Up to 7% of phosphate species in BC-C and BC-N were unidentified by LCF on the XANES spectra. In contrast to biochars, Fe-P was the primary species in FBC-N and FBC-C, accounting for approximately 58% of the total phosphate. The Ca-P was found to be a secondary species (~28%). Notably, Al-P in FBC-N and FBC-C was not identified in the best three results of LCF, corresponding to the much smaller Al concentrations (0.23–0.31%) than those in BC-C and BC-N (Table S3). Overall, Fe-P was the primary species in all the four adsorbents; however, the contribution of Fe-P increased more in the Fe (III) loaded chitosan-biochar composite fibers (i.e., FBC-N and FBC-C).

4. Conclusions

In this study, Fe (III) loaded chitosan-biochar composite fibers (FBC-N and FBC-C) were successfully fabricated using two types of PMS biochars (produced under CO_2 and N_2 environments; BC-N and BC-C, respectively), and evaluated for phosphate removal from aqueous solutions. The SEM-EDS, XPS, Raman spectroscopy, and SSA analysis revealed that the physicochemical and surface morphological properties of the FBCs were significantly different compared to the biochars. FBCs exhibited a greater phosphate adsorption capacity than the other three adsorbents. The solution pH 4.0 and adsorbent dosage 2 g L^{-1} were considered as the optimum conditions for maximizing phosphate removal. The maximum phosphate adsorption (q_m) capacities of BC-N, BC-C, FBC-N, and FBC-C were 9.63, 8.56, 16.43, and 19.24 mg P g^{-1}, respectively, indicating that FBCs had enhanced phosphate adsorption abilities, as compared to pristine biochars. The H^+ transfer, electrostatic attraction, H-bonding complexation, ligand exchange and precipitation mechanisms were involved in the phosphate adsorption. The FBCs thus demonstrated high potential of being green and inexpensive adsorbents for phosphate removal from aqueous solutions. The post-treatment FBCs can be used as potential fertilizers, which could prove to be an ideal method of resource recycling, while conserving the soil and water quality.

Declaration of Conflicts of Interest

The authors declare that they have no known competing financial interests or personal relationships that could appear to influence the work reported in this manuscript.

Acknowledgments

This work was carried out with the support of the Cooperative Research Program for Agriculture Science and Technology Development (Effects of Plastic Mulch Wastes on crop productivity and Agro-Environment, Project No. PJ01475801), Rural Development Administration, Republic of Korea. We would also like to thank Aichi Synchrotron Radiation Center, Aichi Science & Technology Foundation, and Aichi in Japan for the XAFS spectroscopy analysis.

References

Acelas, N.Y., Martin, B.D., López, D., Jefferson, B. 2015. Selective removal of phosphate from wastewater using hydrated metal oxides dispersed within anionic exchange media. *Chemosphere*, **119**, 1353-1360.

Afzal, M.Z., Sun, X.-F., Liu, J., Song, C., Wang, S.-G., Javed, A. 2018. Enhancement of ciprofloxacin sorption on chitosan/biochar hydrogel beads. *Science of The Total Environment*, **639**, 560-569.

Ahmad, M., Lee, S.S., Rajapaksha, A.U., Vithanage, M., Zhang, M., Cho, J.S., Lee, S.-E., Ok, Y.S. 2013. Trichloroethylene adsorption by pine needle biochars produced at various pyrolysis temperatures. *Bioresource technology*, **143**, 615-622.

Araujo, J.R., Archanjo, B.S., de Souza, K.R., Kwapinski, W., Falcão, N.P.S., Novotny, E.H., Achete, C.A. 2014. Selective extraction of humic acids from an anthropogenic Amazonian dark earth and from a chemically oxidized charcoal. *Biology and Fertility of Soils*, **50**(8), 1223-1232.

Aswin Kumar, I., Viswanathan, N. 2018. Development and reuse of amine-grafted chitosan hybrid beads in the retention of nitrate and phosphate. *Journal of Chemical & Engineering Data*, **63**(1), 147-158.

Awual, M.R. 2019. Efficient phosphate removal from water for controlling eutrophication using novel composite adsorbent. *Journal of Cleaner Production*, **228**, 1311-1319.

Awual, M.R., Asiri, A.M., Rahman, M.M., Alharthi, N.H. 2019a. Assessment of enhanced nitrite removal and monitoring using ligand modified stable conjugate materials. *Chemical Engineering Journal*, **363**, 64-72.

Awual, M.R., El-Safty, S.A., Jyo, A. 2011. Removal of trace arsenic (V) and phosphate from water by a highly selective ligand exchange adsorbent. *Journal of Environmental Sciences*, **23**(12), 1947-1954.

Awual, M.R., Hasan, M.M., Asiri, A.M., Rahman, M.M. 2019b. Cleaning the arsenic (V) contaminated water for safe-guarding the public health using novel composite material. *Composites Part B: Engineering*, **171**, 294-301.

Awual, M.R., Hasan, M.M., Khaleque, M.A. 2015. Efficient selenium (IV) detection and removal from water by tailor-made novel conjugate adsorbent. *Sensors and Actuators B: Chemical*, **209**, 194-202.

Awual, M.R., Jyo, A. 2011. Assessing of phosphorus removal by polymeric anion exchangers. *Desalination*, **281**, 111-117.

Awual, M.R., Jyo, A. 2009. Rapid column-mode removal of arsenate from water by crosslinked poly (allylamine) resin. *water research*, **43**(5), 1229-1236.

Awual, M.R., Shenashen, M., Jyo, A., Shiwaku, H., Yaita, T. 2014. Preparing of novel fibrous ligand exchange adsorbent for rapid column-mode trace phosphate removal from water. *Journal of Industrial and Engineering Chemistry*, **20**(5), 2840-2847.

Blaney, L.M., Cinar, S., SenGupta, A.K. 2007. Hybrid anion exchanger for trace phosphate removal from water and wastewater. *Water Research*, **41**(7), 1603-1613.

Bozorgpour, F., Ramandi, H.F., Jafari, P., Samadi, S., Yazd, S.S., Aliabadi, M. 2016. Removal of nitrate and phosphate using chitosan/Al2O3/Fe3O4 composite nanofibrous adsorbent: Comparison with chitosan/Al2O3/Fe3O4 beads. *International journal of biological macromolecules*, **93**, 557-565.

Chatterjee, S., Woo, S.H. 2009. The removal of nitrate from aqueous solutions by chitosan hydrogel beads. *Journal of hazardous materials*, **164**(2-3), 1012-1018.

Cho, D.-W., Kwon, E.E., Kwon, G., Zhang, S., Lee, S.-R., Song, H. 2017a. Co-pyrolysis of paper mill sludge and spend coffee ground using CO2 as reaction medium. *Journal of CO2 Utilization*, **21**, 572-579.

Cho, D.-W., Kwon, E.E., Song, H. 2016. Use of carbon dioxide as a reaction medium in the thermo-chemical process for the enhanced generation of syngas and tuning adsorption ability of biochar. *Energy conversion and management*, **117**, 106-114.

Cho, D.-W., Kwon, G., Yoon, K., Tsang, Y.F., Ok, Y.S., Kwon, E.E., Song, H. 2017b. Simultaneous production of syngas and magnetic biochar via pyrolysis of paper mill sludge using CO2 as reaction medium. *Energy Conversion and Management*, **145**, 1-9.

Cui, X., Dai, X., Khan, K.Y., Li, T., Yang, X., He, Z. 2016. Removal of phosphate from aqueous solution using magnesium-alginate/chitosan modified biochar microspheres derived from Thalia dealbata. *Bioresource technology*, **218**, 1123-1132.

Cui, X., Li, H., Yao, Z., Shen, Y., He, Z., Yang, X., Ng, H.Y., Wang, C.-H. 2019. Removal of nitrate and phosphate by chitosan composited beads derived from crude oil refinery waste: Sorption and cost-benefit analysis. *Journal of cleaner production*, **207**, 846-856.

Delgadillo-Mirquez, L., Lopes, F., Taidi, B., Pareau, D. 2016. Nitrogen and phosphate removal from wastewater with a mixed microalgae and bacteria culture. *Biotechnology Reports*, **11**, 18-26.

Ding, S., Fang, D., Pang, Z., Luo, B., Kuang, L., Wang, H., Zhang, Q., Shen, Q., Ji, F. 2018. Immobilization of powdery calcium silicate hydrate via PVA covalent cross-linking process for phosphorus removal. *Science of The Total Environment*, **645**, 937-945.

El-Naggar, A., El-Naggar, A.H., Shaheen, S.M., Sarkar, B., Chang, S.X., Tsang, D.C.W., Rinklebe, J., Ok, Y.S. 2019. Biochar composition-dependent impacts on soil nutrient release, carbon mineralization, and potential environmental risk: A review. *Journal of Environmental Management*, **241**, 458-467.

Elwakeel, K.Z., Al-Bogami, A.S., Guibal, E. 2021. 2-Mercaptobenzimidazole derivative of chitosan for silver sorption–Contribution of magnetite incorporation and sonication effects on enhanced metal recovery. *Chemical Engineering Journal*, **403**, 126265.

Emmanuelawati, I., Yang, J., Zhang, J., Zhang, H., Zhou, L., Yu, C. 2013. Low-cost and large-scale synthesis of functional porous materials for phosphate removal with high performance. *Nanoscale*, **5**(13), 6173-6180.

Fan, S., Huang, Z., Zhang, Y., Hu, H., Liang, X., Gong, S., Zhou, J., Tu, R. 2019. Magnetic chitosan-hydroxyapatite composite microspheres: Preparation, characterization, and application for the adsorption of phenolic substances. *Bioresource Technology*, **274**, 48-55.

Geng, N., Wu, Y., Zhang, M., Tsang, D.C.W., Rinklebe, J., Xia, Y., Lu, D., Zhu, L., Palansooriya, K.N., Kim, K.-H., Ok, Y.S. 2019. Bioaccumulation of potentially toxic elements by submerged plants and biofilms: A critical review. *Environment International*, **131**, 105015.

Ghods, P., Isgor, O., Brown, J., Bensebaa, F., Kingston, D. 2011. XPS depth profiling study on the passive oxide film of carbon steel in saturated calcium hydroxide solution and the effect of chloride on the film properties. *Applied Surface Science*, **257**(10), 4669-4677.

Goscianska, J., Ptaszkowska-Koniarz, M., Frankowski, M., Franus, M., Panek, R., Franus, W. 2018. Removal of phosphate from water by lanthanum-modified zeolites obtained from fly ash. *Journal of Colloid and Interface Science*, **513**, 72-81.

Hashimoto, Y., Takamoto, A., Kikkawa, R., Murakami, K., Yamaguchi, N. 2014. Formations of hydroxyapatite and inositol hexakisphosphate in poultry litter during the composting period: Sequential fractionation, P K-edge XANES and solution 31P NMR investigations. *Environmental science & technology*, **48**(10), 5486-5492.

Hautier, Y., Zhang, P., Loreau, M., Wilcox, K.R., Seabloom, E.W., Borer, E.T., Byrnes, J.E., Koerner, S.E., Komatsu, K.J., Lefcheck, J.S. 2020. General destabilizing effects of eutrophication on grassland productivity at multiple spatial scales. *Nature communications*, **11**(1), 1-9.

Herath, I., Zhao, F.-J., Bundschuh, J., Wang, P., Wang, J., Ok, Y.S., Palansooriya, K.N., Vithanage, M. 2020. Microbe mediated immobilization of arsenic in the rice rhizosphere after incorporation of silica impregnated biochar composites. *Journal of Hazardous Materials*, **398**, 123096.

Hong, S.U., Ouyang, L., Bruening, M.L. 2009. Recovery of phosphate using multilayer polyelectrolyte nanofiltration membranes. *J. Membr. Sci.*, **327**(1–2), 2.

Hu, S., Ma, X., Lin, Y., Yu, Z., Fang, S. 2015. Thermogravimetric analysis of the co-combustion of paper mill sludge and municipal solid waste. *Energy Conversion and Management*, **99**, 112-118.

Huang, X., Liu, Y., Liu, S., Tan, X., Ding, Y., Zeng, G., Zhou, Y., Zhang, M., Wang, S., Zheng, B. 2016. Effective removal of Cr (VI) using β-cyclodextrin–chitosan modified biochars with adsorption/reduction bifuctional roles. *Rsc Advances*, **6**(1), 94-104.

Huang, Y., Ciais, P., Goll, D.S., Sardans, J., Peñuelas, J., Cresto-Aleina, F., Zhang, H. 2020a. The shift of phosphorus transfers in global fisheries and aquaculture. *Nature communications*, **11**(1), 1-10.

Huang, Y., Lee, X., Grattieri, M., Yuan, M., Cai, R., Macazo, F.C., Minteer, S.D. 2020b. Modified biochar for phosphate adsorption in environmentally relevant conditions. *Chemical Engineering Journal*, **380**, 122375.

Igalavithana, A.D., Kwon, E.E., Vithanage, M., Rinklebe, J., Moon, D.H., Meers, E., Tsang, D.C., Ok, Y.S. 2019. Soil lead immobilization by biochars in short-term laboratory incubation studies. *Environment international*, **127**, 190-198.

Igalavithana, A.D., Yang, X., Zahra, H.R., Tack, F.M., Tsang, D.C., Kwon, E.E., Ok, Y.S. 2018. Metal (loid) immobilization in soils with biochars pyrolyzed in N2 and CO2 environments. *Science of the total environment*, **630**, 1103-1114.

İrdemez, Ş., Demircioğlu, N., Yildiz, Y.Ş. 2006. The effects of pH on phosphate removal from wastewater by electrocoagulation with iron plate electrodes. *Journal of Hazardous Materials*, **137**(2), 1231-1235.

Jang, J., Lee, D.S. 2019. Effective phosphorus removal using chitosan/Ca-organically modified montmorillonite beads in batch and fixed-bed column studies. *Journal of Hazardous Materials*, **375**, 9-18.

Jiang, H., Chen, P., Luo, S., Tu, X., Cao, Q., Shu, M. 2013. Synthesis of novel nanocomposite Fe3O4/ZrO2/chitosan and its application for removal of nitrate and phosphate. *Applied Surface Science*, **284**, 942-949.

Khalil, A.M.E., Eljamal, O., Amen, T.W.M., Sugihara, Y., Matsunaga, N. 2017. Optimized nano-scale zero-valent iron supported on treated activated carbon for enhanced nitrate and phosphate removal from water. *Chemical Engineering Journal*, **309**, 349-365.

Khanday, W.A., Asif, M., Hameed, B.H. 2017. Cross-linked beads of activated oil palm ash zeolite/chitosan composite as a bio-adsorbent for the removal of methylene blue and acid blue 29 dyes. *International Journal of Biological Macromolecules*, **95**, 895-902.

Khare, N., Hesterberg, D., Beauchemin, S., Wang, S.-L. 2004. XANES determination of adsorbed phosphate distribution between ferrihydrite and boehmite in mixtures. *Soil Science Society of America Journal*, **68**(2), 460-469.

Kumar, I.A., Viswanathan, N. 2017. Development of multivalent metal ions imprinted chitosan biocomposites for phosphate sorption. *International Journal of Biological Macromolecules*, **104**, 1539-1547.

Lee, J., Yang, X., Cho, S.-H., Kim, J.-K., Lee, S.S., Tsang, D.C., Ok, Y.S., Kwon, E.E. 2017. Pyrolysis process of agricultural waste using CO2 for waste management, energy recovery, and biochar fabrication. *Applied energy*, **185**, 214-222.

Lei, Y., Narsing, S., Saakes, M., van der Weijden, R.D., Buisman, C.J.N. 2019. Calcium Carbonate Packed Electrochemical Precipitation Column: New Concept of Phosphate Removal and Recovery. *Environmental Science & Technology*, **53**(18), 10774-10780.

Li, G., Gao, S., Zhang, G., Zhang, X. 2014. Enhanced adsorption of phosphate from aqueous solution by nanostructured iron(III)–copper(II) binary oxides. *Chemical Engineering Journal*, **235**, 124-131.

Li, L., Iqbal, J., Zhu, Y., Zhang, P., Chen, W., Bhatnagar, A., Du, Y. 2018. Chitosan/Ag-hydroxyapatite nanocomposite beads as a potential adsorbent for the efficient removal of toxic aquatic pollutants. *International Journal of Biological Macromolecules*, **120**, 1752-1759.

Li, X., Hayashi, J.-i., Li, C.-Z. 2006a. FT-Raman spectroscopic study of the evolution of char structure during the pyrolysis of a Victorian brown coal. *Fuel*, **85**(12-13), 1700-1707.

Li, X., Hayashi, J.-i., Li, C.-Z. 2006b. Volatilisation and catalytic effects of alkali and alkaline earth metallic species during the pyrolysis and gasification of Victorian brown coal. Part VII. Raman spectroscopic study on the changes in char structure during the catalytic gasification in air. *Fuel*, **85**(10-11), 1509-1517.

Liu, X., Zhang, L. 2015. Removal of phosphate anions using the modified chitosan beads: adsorption kinetic, isotherm and mechanism studies. *Powder Technology*, **277**, 112-119.

Liu, Y. 2008. New insights into pseudo-second-order kinetic equation for adsorption. *Colloids and Surfaces A: Physicochemical and Engineering Aspects*, **320**(1), 275-278.

Lou, K., Rajapaksha, A.U., Ok, Y.S., Chang, S.X. 2016. Pyrolysis temperature and steam activation effects on sorption of phosphate on pine sawdust biochars in aqueous solutions. *Chemical Speciation & Bioavailability*, **28**(1-4), 42-50.

Luo, Q., Huang, X., Luo, Y., Yuan, H., Ren, T., Li, X., Xu, D., Guo, X., Wu, Y. 2020. Fluorescent chitosan-based hydrogel incorporating titanate and cellulose nanofibers modified with carbon dots for adsorption and detection of Cr(VI). *Chemical Engineering Journal*, 127050.

Luo, W., Hai, F.I., Price, W.E., Guo, W., Ngo, H.H., Yamamoto, K., Nghiem, L.D. 2016. Phosphorus and water recovery by a novel osmotic membrane bioreactor–reverse osmosis system. *Bioresource Technology*, **200**, 297-304.

Mandal, A., Singh, N. 2016. Kinetic and isotherm error optimization studies for adsorption of atrazine and imidacloprid on bark of Eucalyptus tereticornis L. *Journal of Environmental Science and Health, Part B*, **51**(3), 192-203.

Micháleková-Richveisová, B., Frišták, V., Pipíška, M., Ďuriška, L., Moreno-Jimenez, E., Soja, G. 2017. Iron-impregnated biochars as effective phosphate sorption materials. *Environmental Science and Pollution Research*, **24**(1), 463-475.

Mor, S., Chhoden, K., Ravindra, K. 2016. Application of agro-waste rice husk ash for the removal of phosphate from the wastewater. *Journal of Cleaner Production*, **129**, 673-680.

Neghi, N., Kumar, M., Burkhalov, D. 2019. Synthesis and application of stable, reusable TiO2 polymeric composites for photocatalytic removal of metronidazole: Removal kinetics and density functional analysis. *Chemical Engineering Journal*, **359**, 963-975.

Ng, J., Cheung, W., McKay, G. 2002. Equilibrium studies of the sorption of Cu (II) ions onto chitosan. *Journal of Colloid and Interface Science*, **255**(1), 64-74.

Osifo, P.O., Webster, A., van der Merwe, H., Neomagus, H.W.J.P., van der Gun, M.A., Grant, D.M. 2008. The influence of the degree of cross-linking on the adsorption properties of chitosan beads. *Bioresource Technology*, **99**(15), 7377-7382.

Palansooriya, K.N., Ok, Y.S., Awad, Y.M., Lee, S.S., Sung, J.-K., Koutsospyros, A., Moon, D.H. 2019a. Impacts of biochar application on upland agriculture: A review. *Journal of environmental management*, **234**, 52-64.

Palansooriya, K.N., Yang, Y., Tsang, Y.F., Sarkar, B., Hou, D., Cao, X., Meers, E., Rinklebe, J., Kim, K.-H., Ok, Y.S. 2019b. Occurrence of contaminants in drinking water sources and the potential of biochar for water quality improvement: A review. *Critical Reviews in Environmental Science and Technology*, 1-63.

Rashid, S., Shen, C., Yang, J., Liu, J., Li, J. 2018. Preparation and properties of chitosan–metal complex: Some factors influencing the adsorption capacity for dyes in aqueous solution. *Journal of Environmental Sciences*, **66**, 301-309.

Ravel, B., Newville, M. 2005. ATHENA, ARTEMIS, HEPHAESTUS: data analysis for X-ray absorption spectroscopy using IFEFFIT. *Journal of synchrotron radiation*, **12**(4), 537-541.

Ren, Z., Shao, L., Zhang, G. 2012. Adsorption of Phosphate from Aqueous Solution Using an Iron–Zirconium Binary Oxide Sorbent. *Water, Air, & Soil Pollution*, **223**(7), 4221-4231.

Rusmin, R., Sarkar, B., Liu, Y., McClure, S., Naidu, R. 2015. Structural evolution of chitosan–palygorskite composites and removal of aqueous lead by composite beads. *Applied Surface Science*, **353**, 363-375.

Sheng, G., Zhu, S., Wang, S., Wang, Z. 2016. Removal of dyes by a novel fly ash–chitosan–graphene oxide composite adsorbent. *RSC advances*, **6**(22), 17987-17994.

Tan, G., Mao, Y., Wang, H., Xu, N. 2020. A comparative study of arsenic(V), tetracycline and nitrate ions adsorption onto magnetic biochars and activated carbon. *Chemical Engineering Research and Design*, **159**, 582-591.

Vaidya, P.D., Kenig, E.Y. 2007. CO2-alkanolamine reaction kinetics: a review of recent studies. *Chemical Engineering & Technology: Industrial Chemistry-Plant Equipment-Process Engineering-Biotechnology*, **30**(11), 1467-1474.

Wang, S., Kong, L., Long, J., Su, M., Diao, Z., Chang, X., Chen, D., Song, G., Shih, K. 2018. Adsorption of phosphorus by calcium-flour biochar: Isotherm, kinetic and transformation studies. *Chemosphere*, **195**, 666-672.

Wei, T., Zhang, Q., Wei, X., Gao, Y., Li, H. 2016. A facile and low-cost route to heteroatom doped porous carbon derived from broussonetia papyrifera bark with excellent supercapacitance and CO 2 capture performance. *Scientific reports*, **6**, 22646.

Wen, Z., Zhang, Y., Dai, C. 2014. Removal of phosphate from aqueous solution using nanoscale zerovalent iron (nZVI). *Colloids and Surfaces A: Physicochemical and Engineering Aspects*, **457**, 433-440.

Wu, F.-C., Tseng, R.-L., Juang, R.-S. 2009. Characteristics of Elovich equation used for the analysis of adsorption kinetics in dye-chitosan systems. *Chemical Engineering Journal*, **150**(2), 366-373.

Xiong, W., Tong, J., Yang, Z., Zeng, G., Zhou, Y., Wang, D., Song, P., Xu, R., Zhang, C., Cheng, M. 2017. Adsorption of phosphate from aqueous solution using iron-zirconium modified activated carbon nanofiber: Performance and mechanism. *Journal of Colloid and Interface Science*, **493**, 17-23.

Yamamoto, K., Hashimoto, Y. 2017. Chemical Species of Phosphorus and Zinc in Water-Dispersible Colloids from Swine Manure Compost. *Journal of environmental quality*, **46**(2), 461-465.

Yamamoto, K., Hashimoto, Y., Kang, J., Kobayashi, K. 2018. Speciation of phosphorus zinc and copper in soil and water-dispersible colloid affected by a long-term application of swine manure compost. *Environmental science & technology*, **52**(22), 13270-13278.

Yang, F., Zhang, S., Sun, Y., Tsang, D.C., Cheng, K., Ok, Y.S. 2019. Assembling biochar with various layered double hydroxides for enhancement of phosphorus recovery. *Journal of hazardous materials*, **365**, 665-673.

Yang, X., Igalavithana, A.D., Oh, S.-E., Nam, H., Zhang, M., Wang, C.-H., Kwon, E.E., Tsang, D.C., Ok, Y.S. 2018a. Characterization of bioenergy biochar and its utilization for metal/metalloid immobilization in contaminated soil. *Science of the total environment*, **640**, 704-713.

Yang, X., Kwon, E.E., Dou, X., Zhang, M., Kim, K.-H., Tsang, D.C., Ok, Y.S. 2018b. Fabrication of spherical biochar by a two-step thermal process from waste potato peel. *Science of the total environment*, **626**, 478-485.

Yang, Y., Lohwacharin, J., Takizawa, S. 2014. Hybrid ferrihydrite-MF/UF membrane filtration for the simultaneous removal of dissolved organic matter and phosphate. *Water Research*, **65**, 177-185.

Yao, Y., Gao, B., Chen, J., Yang, L. 2013. Engineered biochar reclaiming phosphate from aqueous solutions: mechanisms and potential application as a slow-release fertilizer. *Environmental science & technology*, **47**(15), 8700-8708.

Yoon, K., Cho, D.-W., Tsang, D.C., Bolan, N., Rinklebe, J., Song, H. 2017. Fabrication of engineered biochar from paper mill sludge and its application into removal of arsenic and cadmium in acidic water. *Bioresource technology*, **246**, 69-75.

Zhang, B., Chen, N., Feng, C., Zhang, Z. 2018a. Adsorption for phosphate by crosslinked/non-crosslinked-chitosan-Fe (III) complex sorbents: characteristic and mechanism. *Chemical Engineering Journal*, **353**, 361-372.

Zhang, H., Zhang, L.M. 2010. Improving the dyeing properties and softness of hemp fabric using chitosan and epoxy modified silicone oil. *The Journal of The Textile Institute*, **101**(9), 849-857.

Zhang, M.-m., Liu, Y.-g., Li, T.-t., Xu, W.-h., Zheng, B.-h., Tan, X.-f., Wang, H., Guo, Y.-m., Guo, F.-y., Wang, S.-f. 2015. Chitosan modification of magnetic biochar produced from

Eichhornia crassipes for enhanced sorption of Cr (VI) from aqueous solution. *RSC Advances*, **5**(58), 46955-46964.

Zhang, M., Song, G., Gelardi, D.L., Huang, L., Khan, E., Mašek, O., Parikh, S.J., Ok, Y.S. 2020. Evaluating biochar and its modifications for the removal of ammonium, nitrate, and phosphate in water. *Water Research*, **186**, 116303.

Zhang, W., Zhang, S., Wang, J., Wang, M., He, Q., Song, J., Wang, H., Zhou, J. 2018b. Hybrid functionalized chitosan-Al2O3@SiO2 composite for enhanced Cr(VI) adsorption. *Chemosphere*, **203**, 188-198.

Zhang, Y., Desmidt, E., Van Looveren, A., Pinoy, L., Meesschaert, B., Van der Bruggen, B. 2013. Phosphate Separation and Recovery from Wastewater by Novel Electrodialysis. *Environmental Science & Technology*, **47**(11), 5888-5895.

Zhang, Z., Yan, L., Yu, H., Yan, T., Li, X. 2019. Adsorption of phosphate from aqueous solution by vegetable biochar/layered double oxides: Fast removal and mechanistic studies. *Bioresource Technology*, **284**, 65-71.

Zhao, T., Feng, T. 2016. Application of modified chitosan microspheres for nitrate and phosphate adsorption from aqueous solution. *RSC Advances*, **6**(93), 90878-90886.

Table captions

Table 1. Selected surface characteristics of BC-N, BC-C, FBC-N, and FBC-C.

Table 2. Estimated adsorption isotherm model parameters for phosphate adsorption onto BC-N, BC-C, FBC-N, and FBC-C.

Table 3. Estimated kinetic model parameters for phosphate adsorption onto BC-N, BC-C, FBC-N, and FBC-C.

Figure captions

Fig. 1. XPS C1s deconvolution spectra of (a) BC-N, (b) BC-C, (c) FBC-N, and (d) FBC-C.

Fig. 2. XPS N1s deconvolution spectra of (a) BC-N, (b) BC-C, (c) FBC-N, and (d) FBC-C.

Fig. 3. Raman deconvolution spectra of (a) BC-N, (b) BC-C, (c) FBC-N, and (d) FBC-C.

Fig. 4. Phosphate adsorption isotherm of BC-N, BC-C, FBC-N, and FBC-C (initial phosphate concentration = 10 to 70 mg P L^{-1}, sorbent dosage = 2 g L^{-1}, temperature = 25 °C, pH = 4, equilibrium time = 24 h) .

Fig. 5. Separation factor (R_L) obtained from the Langmuir model against initial phosphate concentrations (C_o) in water for BC-N, BC-C, FBC-N, and FBC-C.

Fig. 6. Phosphate adsorption kinetics of BC-N, BC-C, FBC-N, and FBC-C (initial phosphate concentration = 40 mg P L^{-1}, sorbent dosage = 2 g L^{-1}, temperature = 25 °C, pH = 4).

Fig. 7. Effect of pH on phosphate removal efficiency by BC-N, BC-C, FBC-N, and FBC-C.

Fig. 8. P K-edge XANES spectra of (a) BC-N, (b) BC-C, (c) FBC-N, and (d) FBC-C. The black solid lines represent the linear combination fits (LCF) using P reference spectra.

Table 1. Selected surface characteristics BC-N, BC-C, FBC-N, and FBC-C.

Sample	BC-N	BC-C	FBC-N	FBC-C
Surface area ($cm^2\ g^{-1}$)	50.58	46.02	7.30	12.30
Pore volume ($cm^3\ g^{-1}$)	0.108	0.107	0.005	0.013
Pore size (nm)	11.90	11.67	1.014	1.877
Porosity (%)	17.59	21.08	3.19	2.77

Biochar produced under N_2 environment (BC-N) and CO_2 environment (BC-C), and respective biochar-chitosan fibers (FBC-N and FBC-C).

Table 2. Estimated adsorption isotherm model parameters for phosphate adsorption onto BC-N, BC-C, FBC-N, and FBC-C.

Isothermal model	Parameters	Unit	BC-N	BC-C	FBC-N	FBC-C
Freundlich	K_f	$mg\ g^{-1}) (L\ mg^{-1})^{1/n}$	0.062	0.041	1.28	3.72
	1/n	$L\ g^{-1}$	1.15	1.02	0.67	0.39
	R^2		0.89	0.68	0.93	0.82
	R^2_{adj}		0.88	0.66	0.92	0.81
	RMSEP		0.80	0.70	1.10	1.75
	RPD		2.37	1.22	3.55	2.01
Langmuir	q_m	$mg\ P\ g^{-1}$	9.63	8.56	16.43	19.24
	b	$L\ mg^{-1}$	0.023	0.009	0.071	0.103
	R^2		0.69	0.71	0.82	0.89
	R^2_{adj}		0.67	0.69	0.81	0.88
	RMSEP		1.22	0.67	1.80	1.36
	RPD		0.98	1.25	1.52	2.75
Sips	q_m	$mg\ P\ g^{-1}$	8.49	7.13	15.04	17.17
	K_s	$L\ mg^{-1}$	0.001	0.013	0.015	0.051
	1/n		1.92	0.99	1.89	1.51
	R^2		0.86	0.66	0.75	0.87
	R^2_{adj}		0.84	0.62	0.73	0.86
	RMSEP		0.82	0.72	2.11	1.47
	RPD		2.18	1.18	1.77	2.92
Redlich–Peterson	K_R	$L\ g^{-1}$	0.33	0.19	0.57	1.29
	αR	$L\ mg^{-1}$	1.99	2.52	0.00009	0.008
	g		0	0	2.36	1.54
	R^2		0.85	0.77	0.97	0.92
	R^2_{adj}		0.84	0.75	0.96	0.91
	RMSEP		0.84	0.59	0.73	1.19
	RPD		2.06	1.72	5.72	3.38

Biochar produced under N_2 environment (BC-N) and CO_2 environment (BC-C), and respective biochar-chitosan fibers (FBC-N and FBC-C).

Table 3. Estimated kinetic model parameters for phosphate adsorption onto BC-N, BC-C, FBC-N, and FBC-C.

Models	Parameters	Unit	BC-N	BC-C	FBC-N	FBC-C
Pseudo-first- order	q_e	mg P g^{-1}	2.09	1.11	9.22	12.69
	k_1	min^{-1}	0.005	0.002	0.021	0.018
	R^2		0.92	0.79	0.92	0.85
	R^2_{adj}		0.91	0.77	0.91	0.84
	RMSEP		0.22	0.18	0.81	1.53
	RPD		3.41	1.98	3.87	2.86
Pseudo-second-order	q_e	mg P g^{-1}	2.39	0.06	10.04	13.87
	k_2	gmg^{-1} min^{-1}	0.003	0.04	0.003	0.002
	R^2		0.92	0.78	0.97	0.93
	R^2_{adj}		0.91	0.77	0.96	0.92
	RMSEP		0.22	0.18	0.55	1.03
	RPD		3.26	1.92	5.40	3.99
Elovich	α	mg g^{-1} min^{-1}	0.10	0.02	1.56	1.83
	β	g mg^{-1}	2.62	5.68	0.67	0.48
	R^2		0.89	0.71	0.93	0.95
	R^2_{adj}		0.88	0.69	0.92	0.94
	RMSEP		0.25	0.21	0.76	0.88
	RPD		2.55	1.30	3.58	4.33
Intra-particle diffusion	k_{id}	mg g^{-1} $min^{-1/2}$	0.06	0.03	0.21	0.31
	θ	mg g^{-1}	0.20	-0.03	3.85	4.85
	R^2		0.80	0.77	0.66	0.74
	R^2_{adj}		0.78	0.75	0.64	0.73
	RMSEP		0.34	0.19	1.66	2.02
	RPD		1.94	1.79	1.37	1.67

Biochar produced under N_2 environment (BC-N) and CO_2 environment (BC-C), and respective biochar-chitosan fibers (FBC-N and FBC-C).

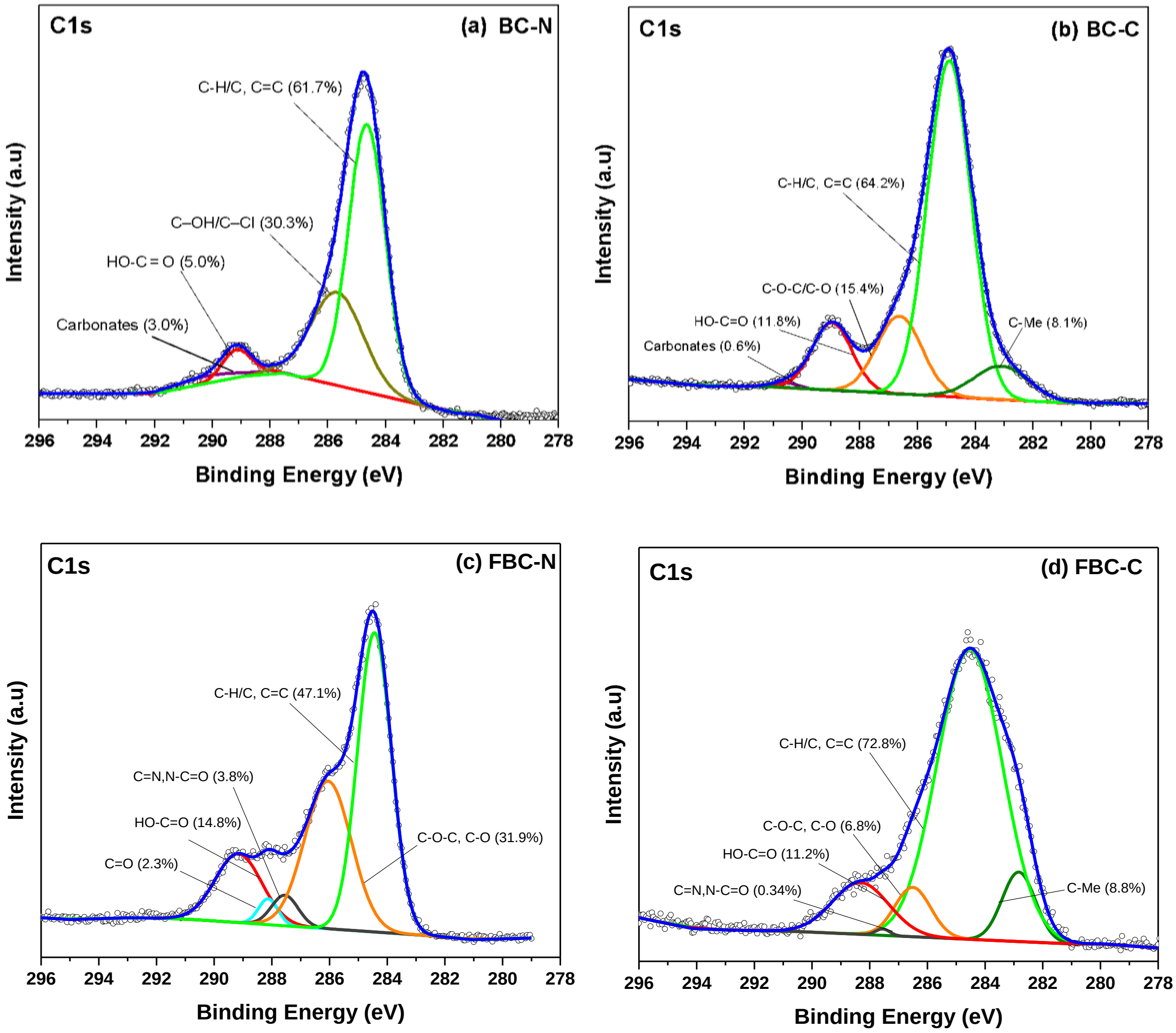

Fig. 1. XPS C1s deconvolution spectra of (a) BC-N), (b) BC-C, (c) FBC-N, and (d) FBC-C).

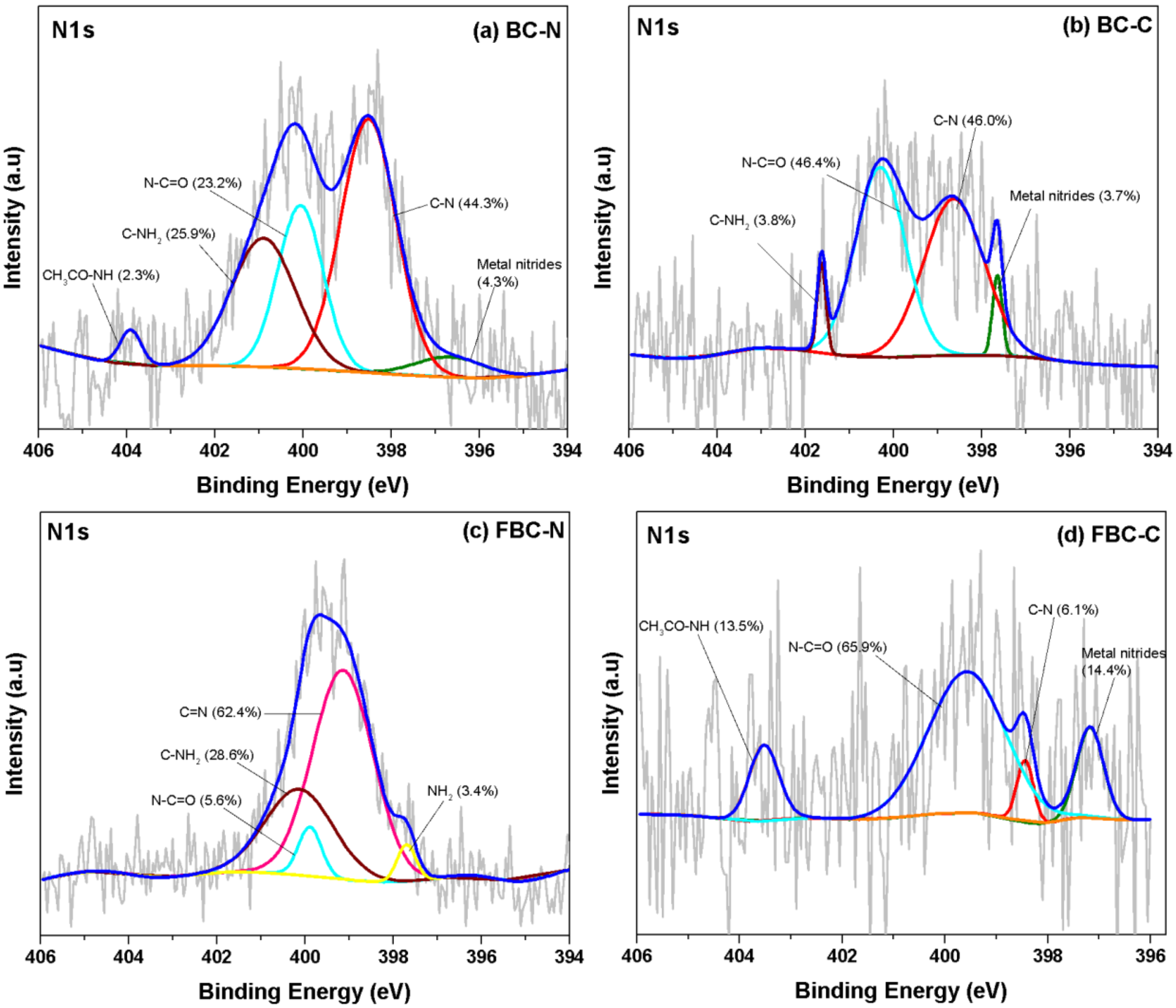

Fig. 2. XPS N1s deconvolution spectra of (a) BC-N, (b) BC-C, (c) FBC-N, and (d) FBC-C).

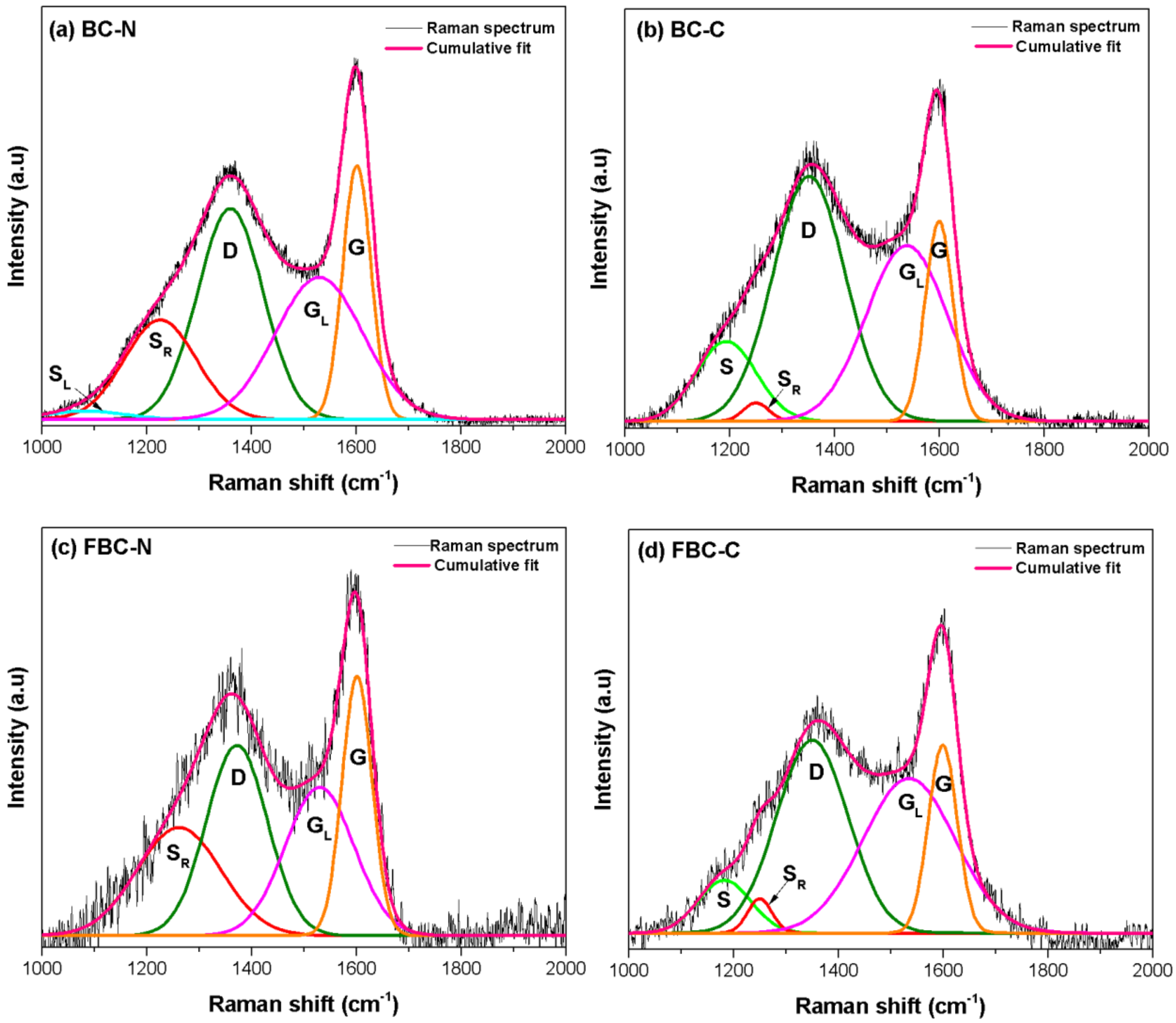

Fig. 3. Raman deconvolution spectra of (a) BC-N, (b) BC-C, (c) FBC-N, and (d) FBC-C).

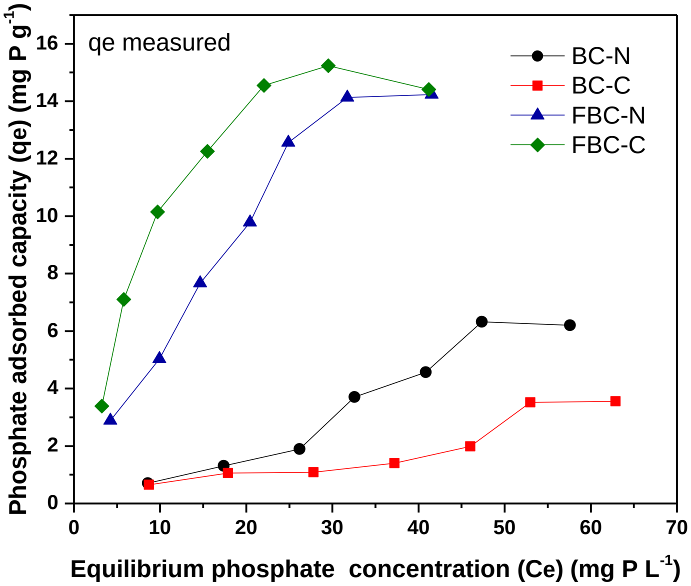

Fig. 4. Phosphate adsorption isotherm of BC-N, BC-C, FBC-N, and FBC-C (initial phosphate concentration = 10 to 70 mg P L^{-1}, sorbent dosage = 2 g L^{-1}, temperature = 25 °C, pH = 4, equilibrium time = 24 h).

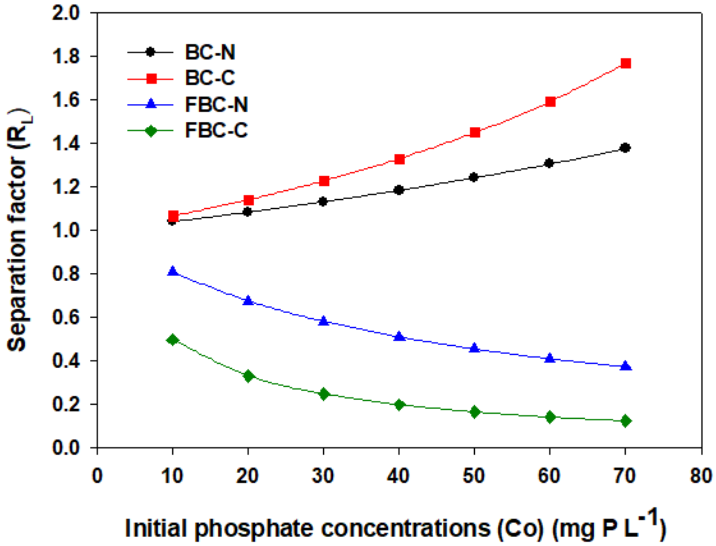

Fig. 5. Separation factor (R_L) obtained from the Langmuir model against initial phosphate concentrations (C_o) in water BC-N, BC-C, FBC-N, and FBC-C.

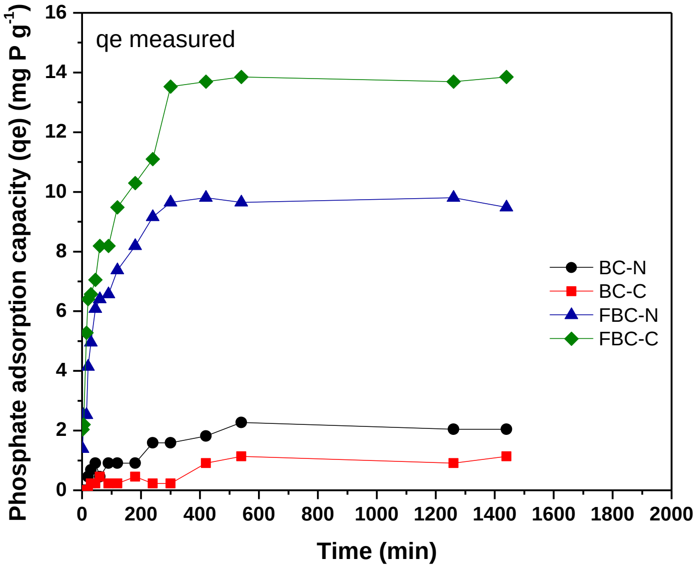

Fig. 6. Phosphate adsorption kinetics of BC-N, BC-C, FBC-N, and FBC-C (initial phosphate concentration = 40 mg P L^{-1}, sorbent dosage = 2 g L^{-1}, temperature = 25 °C, pH = 4).

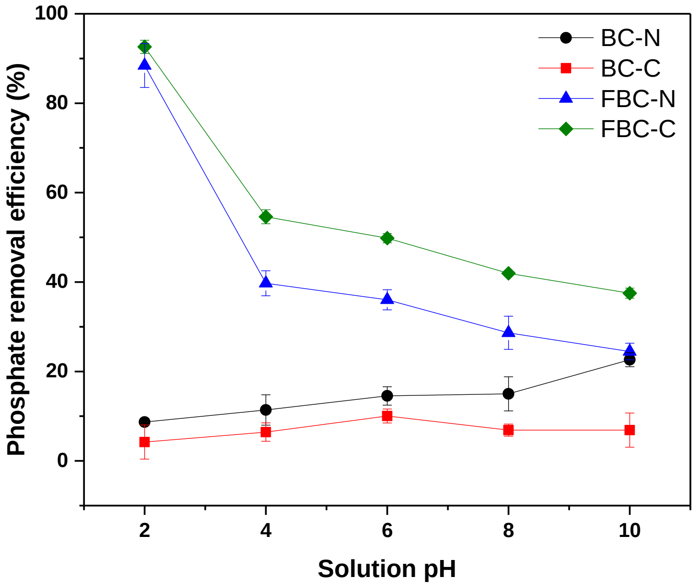

Fig. 7. Effect of pH on phosphate removal efficiency by BC-N, BC-C, FBC-N, and FBC-C.

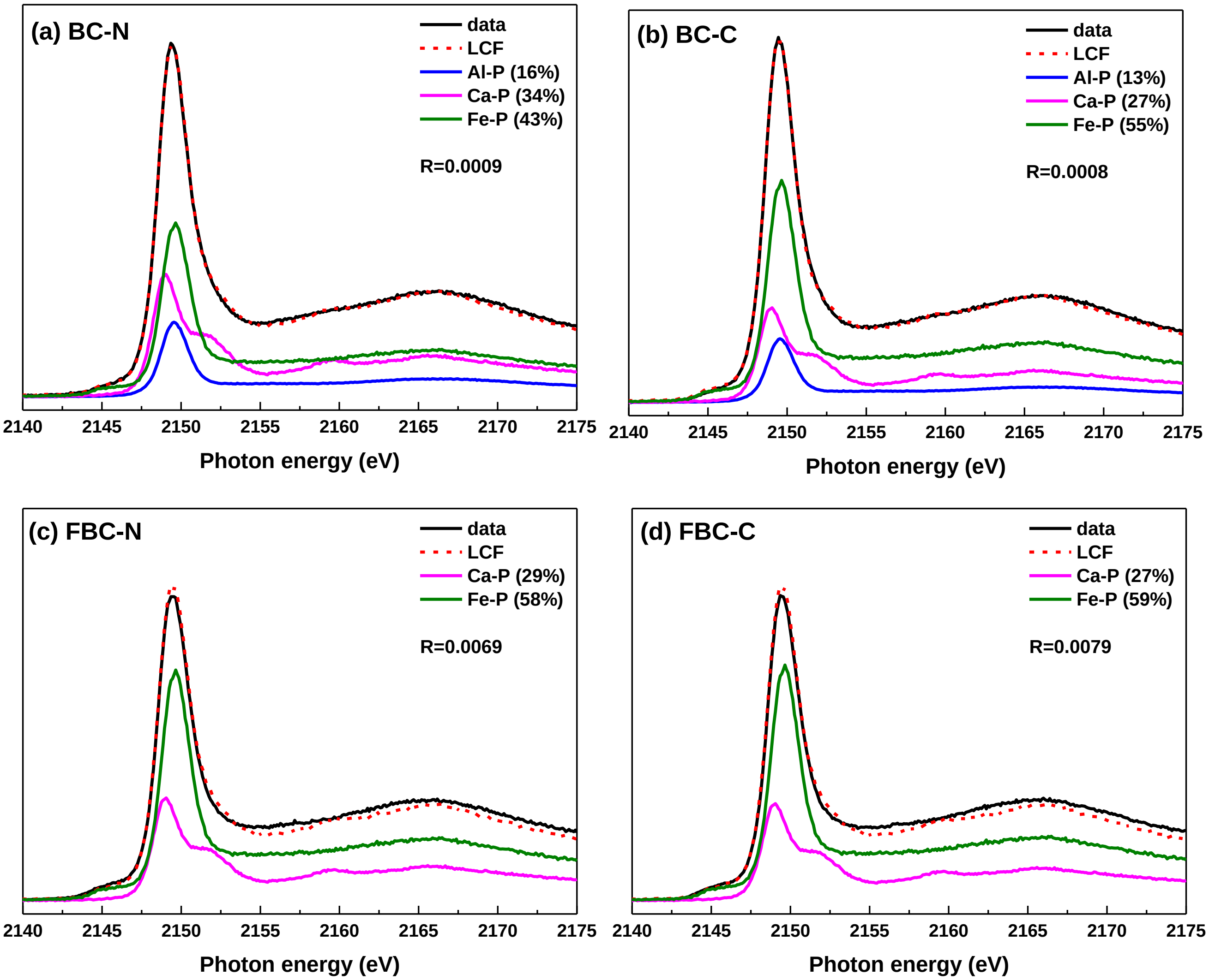

Fig. 8. P K-edge XANES spectra of (a) BC-N, (b) BC-C, (c) FBC-N, and (d) FBC-C. The black solid lines represent the linear combination fits (LCF) using P reference spectra.

Supporting Information

Fe(III) Loaded Chitosan-Biochar Composite Fibers for the Removal of Phosphate from Water

Kumuduni Niroshika Palansooriya[a,1], Sok Kim[b,1], Avanthi Deshani Igalavithana[a,c], Yohey Hashimoto[d], Yoon-E Choi[b], Raj Mukhopadhyay[e], Binoy Sarkar[f], Yong Sik Ok[a,*]

[a] *Korea Biochar Research Center, APRU Sustainable Waste Management Program & Division of Environmental Science and Ecological Engineering, Korea University, Seoul 02841, South Korea*

[b] *Division of Environmental Science and Ecological Engineering, Korea University, Seoul 02841, Republic of Korea*

[c] *Department of Soil Science, Faculty of Agriculture, University of Peradeniya, 20400, Peradeniya, Sri Lanka*

[d] *Department of Bioapplications and Systems Engineering, Tokyo University of Agriculture and Technology, Tokyo 184-8588, Japan*

[e] *Division of Irrigation and Drainage Engineering, ICAR- Central Soil Salinity Research Institute, Karnal 132001, Haryana, India*

[f] *Lancaster Environment Centre, Lancaster University, Lancaster LA1 4YQ, United Kingdom*

*Corresponding author:

Prof. Yong Sik Ok, Korea University. E-mail: yongsikok@korea.ac.kr. Tel: +82-2-3290-3044

---

[1] These authors share co-first authorship.

1. *Adsorption Isothermal models*

The phosphate adsorption isotherm data obtained from various experiments were fitted to Langmuir, Freundlich, Sips and Redlich–Peterson isotherm equations by non-linear regression using the least square method. The empirical equations are detailed below.

Langmuir isotherm: $q_e = (b\ C_e\ q_m)/\ (1 + b\ C_e)$ (Eq. 1)

Freundlich isotherm: $q_e = K_f\ C_e^{1/n}$ (Eq. 2)

Sips isotherm: $q_e = (q_m\ K_s\ C_e^{1/n})/\ (1 + K_s\ C_e^{1/n})$ (Eq. 3)

Redlich–Peterson isotherm: $q_e = (K_R\ C_e)\ /\ (1 + \alpha R\ C_e^{g})$ (Eq. 4)

where, C_e (mg P L^{-1}) is the equilibrium concentration of phosphate; q_m is the potential adsorption maxima of the biochar adsorbents (mg P g^{-1}); b is the bonding energy constant (L mg^{-1}); K_f [(mg g^{-1}) (L mg^{-1})$^{1/n}$] and 1/n (L g^{-1}) are the Freundlich constant at equilibrium and exponential factor, respectively; K_s indicates the affinity of constant for adsorption (L mg^{-1}); K_R, is the adsorption capacity constant (L g^{-1}); αR and g are the isotherm constant (L mg^{-1}) and the exponential factor, respectively.

The thermodynamic characteristics of the Langmuir isotherm model were evaluated using the separation factor (R_L) to determine the favorable adsorption process. The R_L value was calculated using Eq. 5 as follows:

$R_L = 1/\ (1 + K_L C_o)$ (Eq. 5)

where, K_L is the Langmuir affinity constant (L g^{-1}).

2. *Adsorption kinetic models*

The kinetic phosphate adsorption data obtained from various experiments were fitted to pseudo-first order, pseudo-second order, intra-particle diffusion, and Elovich models by non-linear regression using the least squares method. The empirical equations are as follows:

Pseudo-first order: $q_t = q_e\ (1 - e^{-k_1 t})$ (Eq. 6)

Pseudo-second order: $q_t = q_e^2\ k_2\ t/\ 1 + q_e\ k_2\ t$ (Eq. 7)

Intra-particle diffusion: $q_t = k_{id} t^{1/2} + \theta$ (Eq. 8)

Elovich: $q_t = 1/\beta \ln(\alpha\beta) + (1/\beta) \ln t$ (Eq. 9)

where, q_e is the equilibrium amount of adsorption of phosphate on the biochar adsorbents (mg P g^{-1}); k_1 is the rate constant of pseudo first-order adsorption (min^{-1}); k_2 is the equilibrium rate constant of pseudo second-order (g mg^{-1} min^{-1}); k_{id} is the rate constant (mg $g^{-1}min^{-1/2}$); θ (mg g^{-1},) is the intercept. α is the sorption rate (mg g^{-1} min^{-1},) and β is the desorption constant (g mg^{-1}) during the experiment.

3. *Data modeling*

The details of the formula for the coefficient of determination (R^2) (Eq. 10), adjusted coefficient of determination (R^2_{adj}) (Eq. 11), root mean square error of prediction (RMSEP) (Eq. 12), and the ratio of performance to the deviation (RPD) are given below.

$R^2 = 1- [(\sum_i^n (q_{e'meas} - q_{e'calc})^2) \div (\sum_i^n (q_{e'meas} - q_{e'meas\ mean})^2)]$ (Eq. 10)

$R^2_{adj} = 1- (1- R^2). \frac{(n-1)}{(n-p)}$ (Eq. 11)

$RMSEP = \sqrt{\frac{1}{n-1}} \sum_i^n (q_{e'meas} - {calc})^2$ (Eq. 12)

RPD = SD/RMSEP (Eq. 13)

where, n = no. of data points; p = no. of parameters in the model equation

Table S1: Assignments of characteristic peaks deconvoluted from the Raman spectra.

Band name	Position (cm^{-1})	Assignment	Reference
S_R	1226–1262	Aryl–alkyl ether; para-aromatics	(Lin-Vien et al., 1991)
S	1183–1194	C_{alkyl}–C_{aryl} and $-CH_3$ on aromatic rings	(Li et al., 2006; Nemanich et al., 1988)
S_L	1084	C–H on aromatic rings; benzene (ortho-di-substituted) ring	(Lin-Vien et al., 1991)
D	1350–1372	Aromatics with no less than 6 rings but less rings than graphite	(Yang et al., 2018)
G	1599–1601	sp^2-bonded graphite crystallite and alkene C=C	(Li et al., 2006)
G_L	1530–1538	Aromatics with 3–5 rings and amorphous carbon	(Li et al., 2006; Yang et al., 2018)

Table S2. Ratio of integrated intensity (peak area (A)) of different peaks in Raman spectra for BC-N, BC-C, FBC-N, and FBC-C.

Sample	A_D/A_G	A_S/A_G
BC-N	1.93	-
BC-C	3.16	0.86
FBC-N	1.50	-
FBC-C	2.54	0.51

Biochar produced under N_2 environment (BC-N) and CO_2 environment (BC-C), and respective biochar-chitosan fibers (FBC-N and FBC-C).

Table S3: Results of binary and ternary combinations of linear combination fit (LCF) on P K-edge XANES spectra of BC-N, BC-C, FBC-N, and FBC-C. The values in bold characters are used for the interpretation of LCF results.

Sample	hydroxyapatite $Ca_5(PO_4)_3OH$	P-ferrihydrite	$Ca_3(PO_4)_2$	P-gibbsite	Strengite $FePO_4 \cdot 2H_2O$	Variscite $AlPO_4 \cdot 2H_2O$	Sum	R-factor
				%				
BC-N	33	62					95	0.0014
		63	29				91	0.0017
	39			50			89	0.0038
	34	**43**		**16**			**93**	**0.0009**
BC-C	26	71					97	0.0012
		72	22				94	0.0014
	32			58			90	0.0053
	27	**55**		**13**			**95**	**0.0008**
FBC-N	**29**	**58**					**86**	**0.0069**
		61	22				83	0.0126
			35		52		87	0.0156
	28	50				10	88	0.0055
FBC-C	**27**	**59**					**86**	**0.0079**
		63	20				83	0.0137
			33		53		87	0.0158
	27	49				13	89	0.0056

R-factor is a residual value for fitting; $R = \Sigma(\mu_{exp} - \mu_{model})^2 / \Sigma(\mu_{exp})^2$

P-gibbsite, P-ferrihydrite: phosphate adsorbed on gibbsite, and ferrihydrite, respectively

Biochar produced under N_2 environment (BC-N) and CO_2 environment (BC-C), and respective biochar-chitosan fibers (FBC-N and FBC-C).

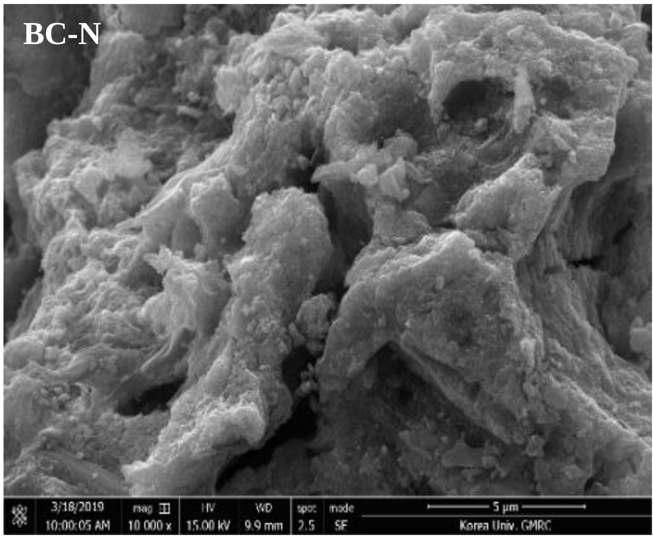

Element	Weight %	Atom %
C	17.66	34.06
O	26.52	38.39
Na	0.43	0.44
Mg	0.61	0.58
Al	1.54	1.32
Si	1.14	0.94
P	1.25	0.93
S	2.00	1.44
Cl	0.82	0.53
Ca	8.73	5.05
Fe	39.30	16.30

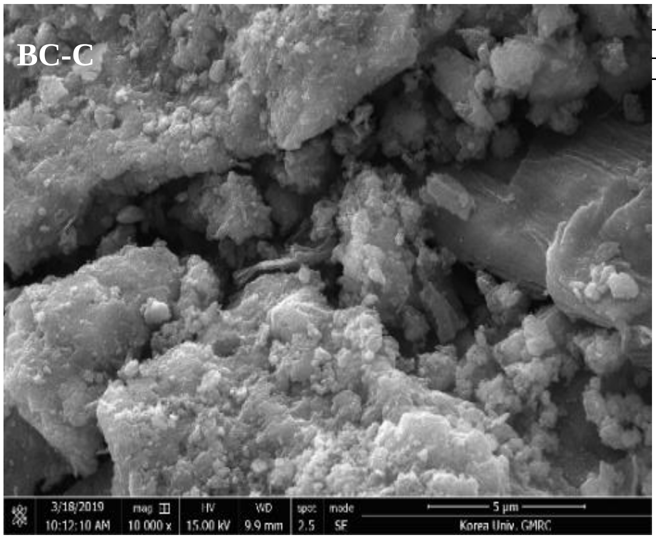

Element	Weight %	Atom %
C	10.65	24.16
O	21.57	36.74
Na	0.53	0.63
Mg	0.69	0.78
Al	1.66	1.68
Si	1.16	1.12
P	1.40	1.23
S	2.31	1.96
Cl	0.99	0.76
Ca	11.08	7.53
Mn	0.69	0.34
Fe	47.25	23.05

Fig. S1. SEM images and SEM-EDS elemental composition of BC-N and BC-C

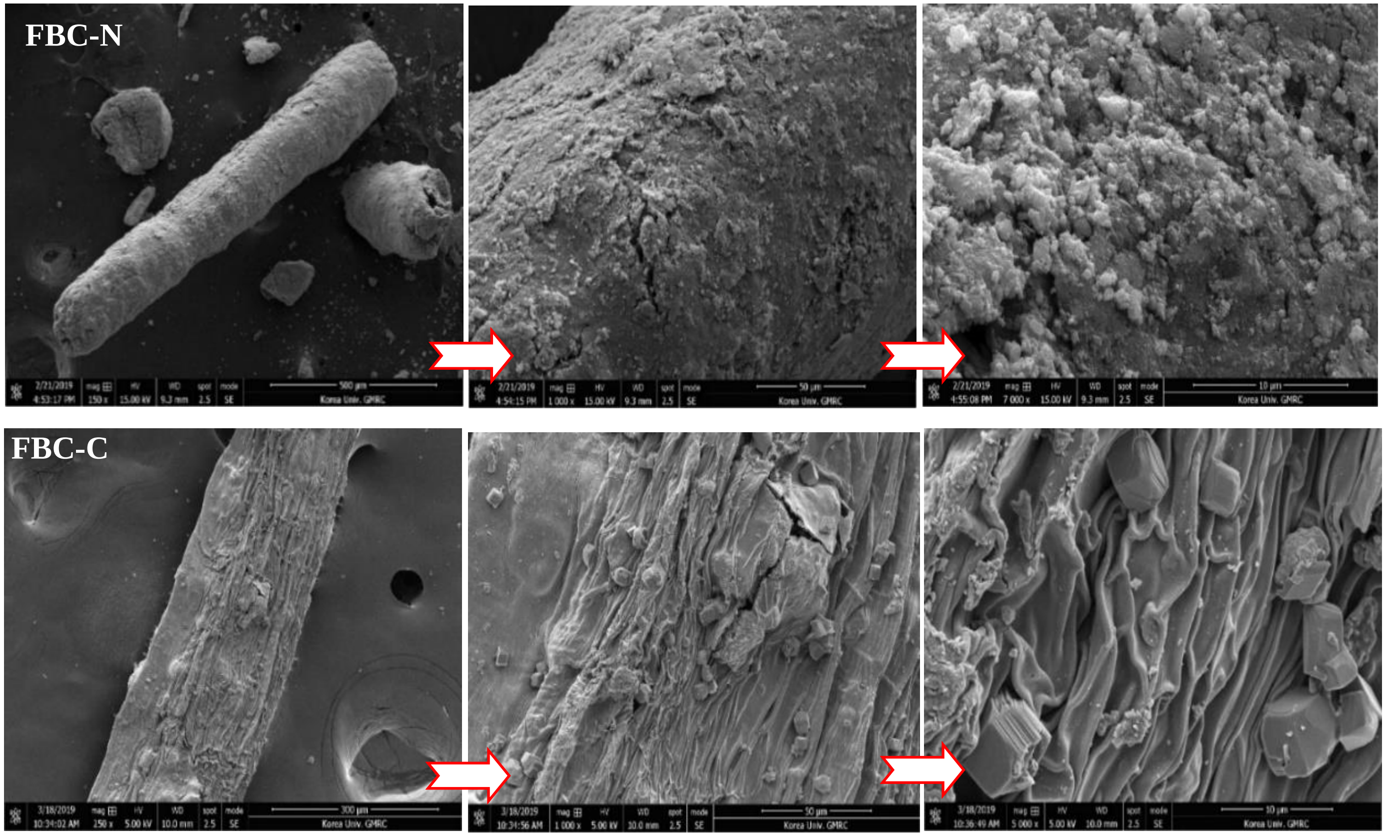

Element	Weight %	Atom %
C	11.43	20.67
N	3.95	6.13
O	38.49	52.27
Na	0.33	0.31
Al	0.31	0.25
Si	0.45	0.35
P	0.69	0.49
S	0.16	0.11
Ca	14.55	7.89
Fe	29.65	11.53

Element	Weight %	Atom %
C	7.16	16.04
N	2.09	4.02
O	28.37	47.72
Na	0.33	0.39
Al	0.23	0.23
Si	0.45	0.43
P	0.83	0.72
Ca	6.74	4.53
Fe	53.79	25.92

Fig. S2. SEM images and SEM-EDS elemental composition of FBC-N and FBC-C.

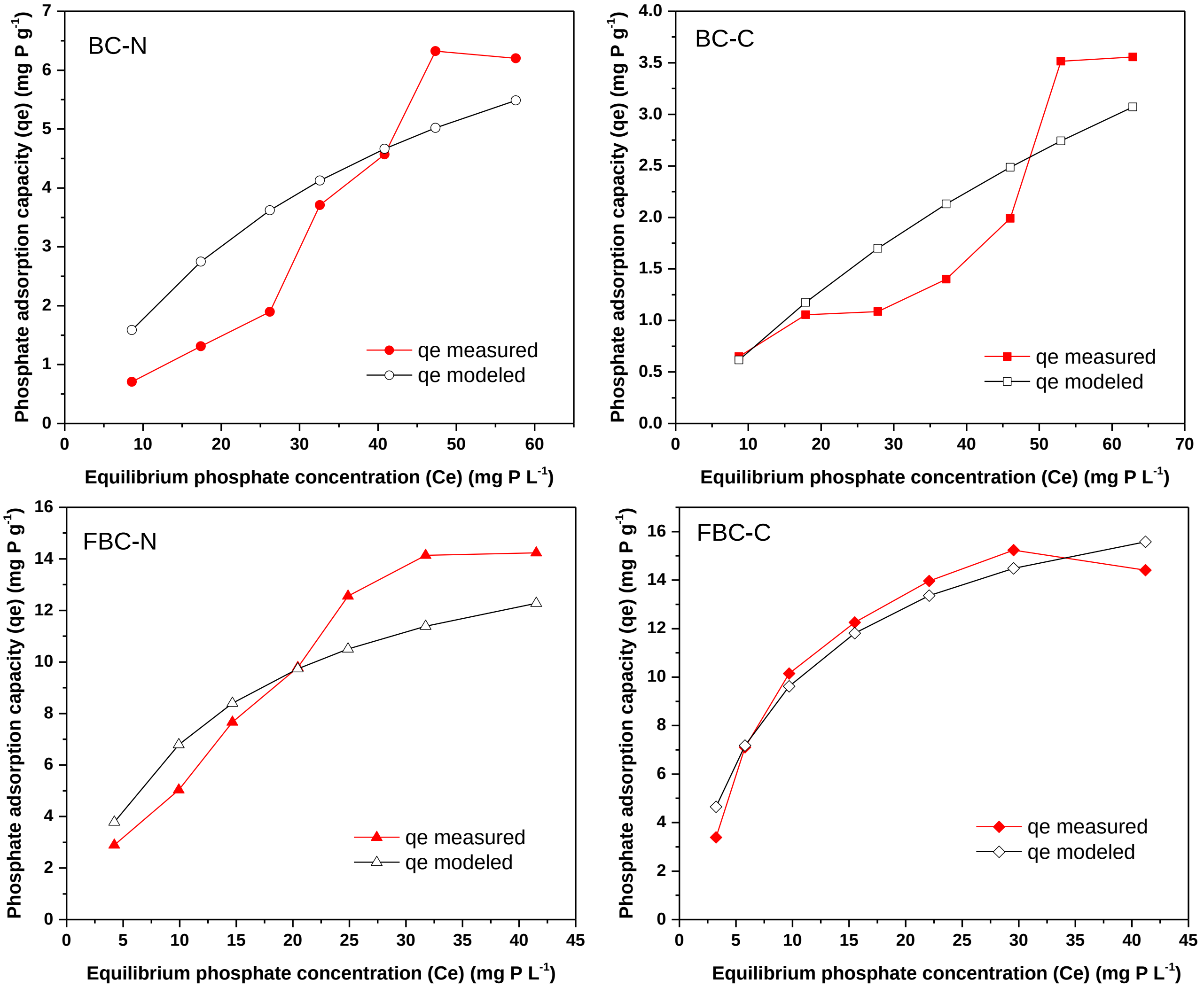

Fig. S3. Non-linear fitting of the Langmuir isotherm model for phosphate adsorption onto BC-N, BC-C, FBC-N, and FBC-C.

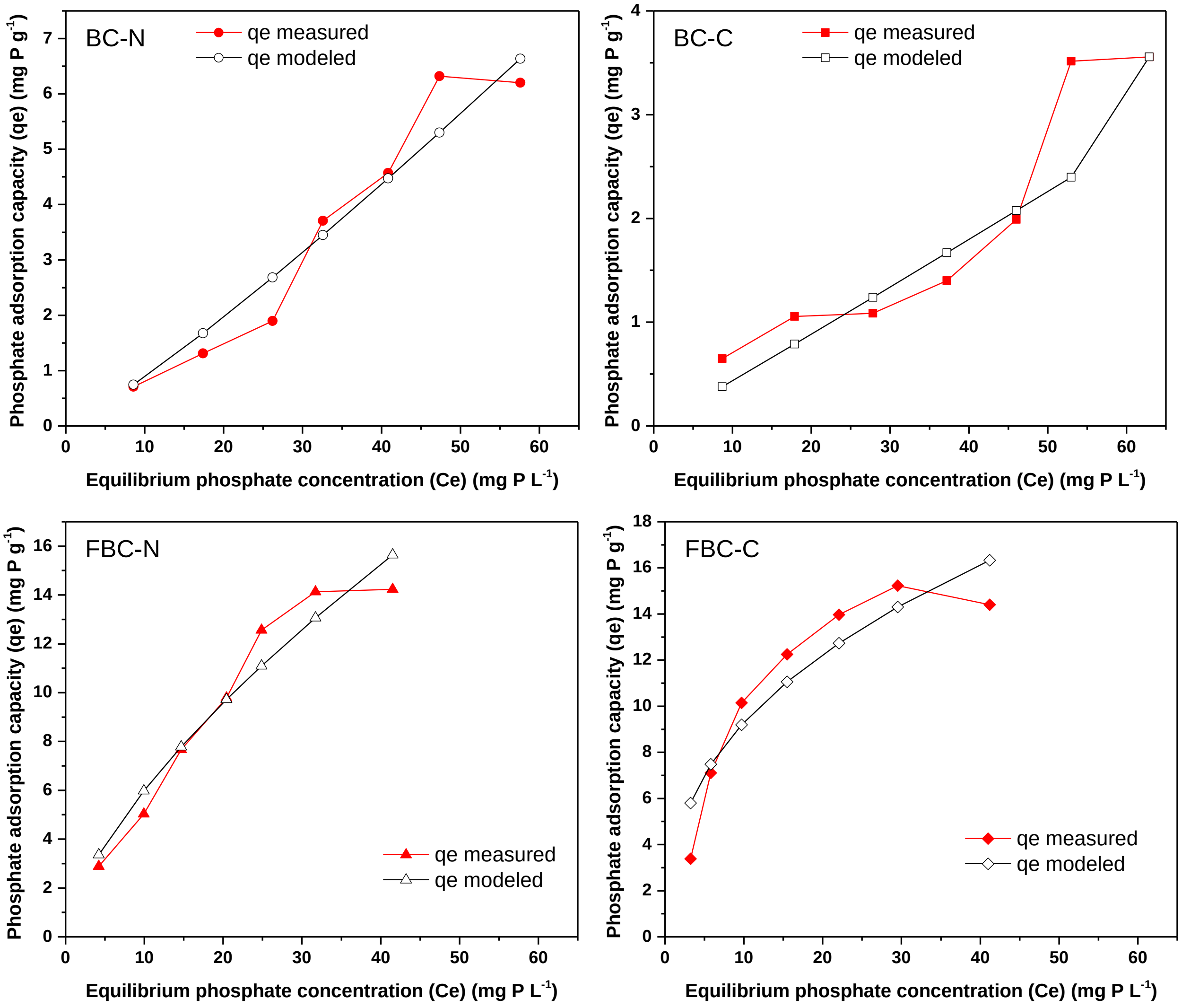

Fig. S4. Non-linear fitting of the Freundlich isotherm model for phosphate adsorption BC-N, BC-C, FBC-N, and FBC-C.

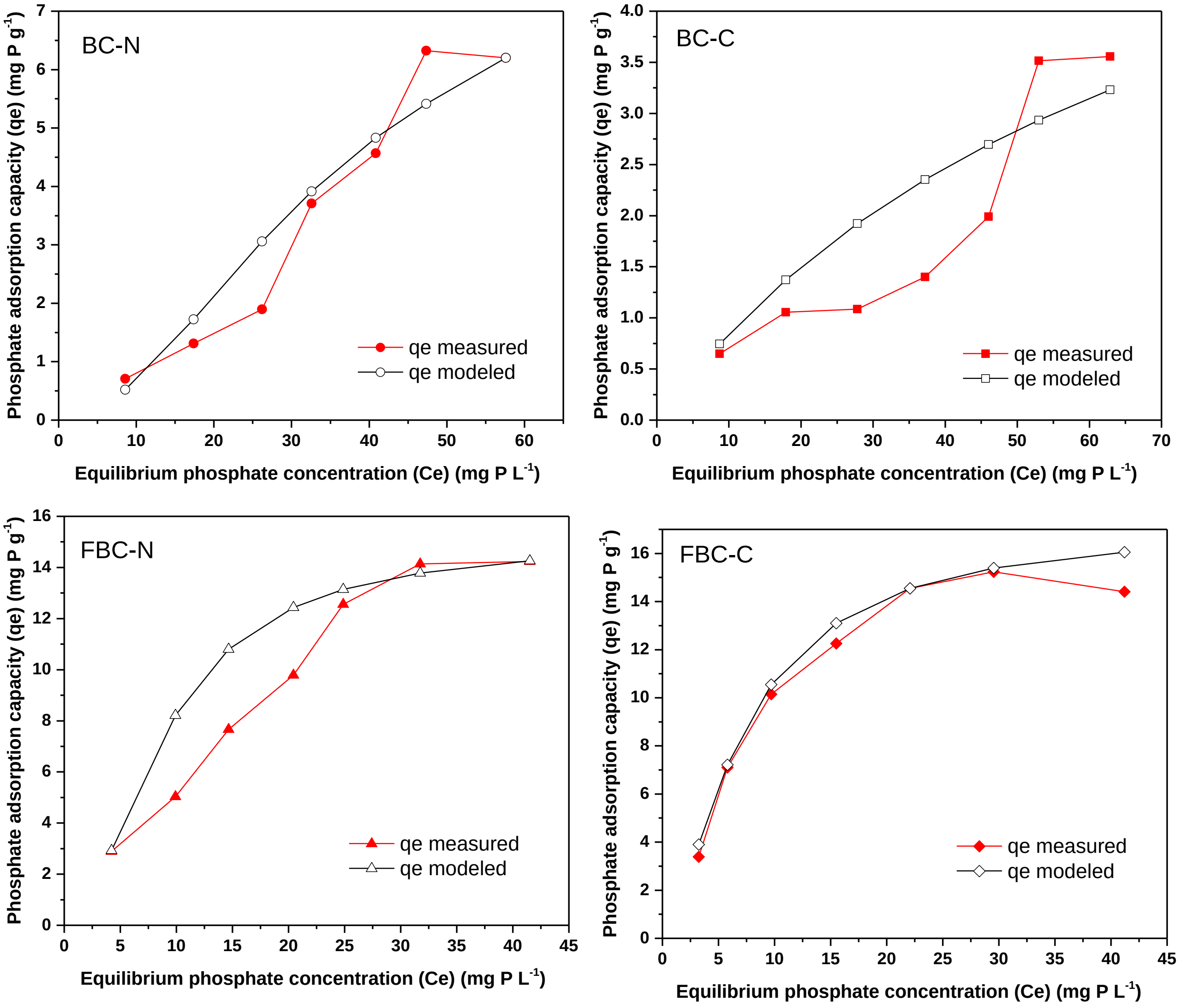

Fig. S5. Non-linear fitting of the Sips isotherm model for phosphate adsorption onto BC-N, BC-C, FBC-N, and FBC-C.

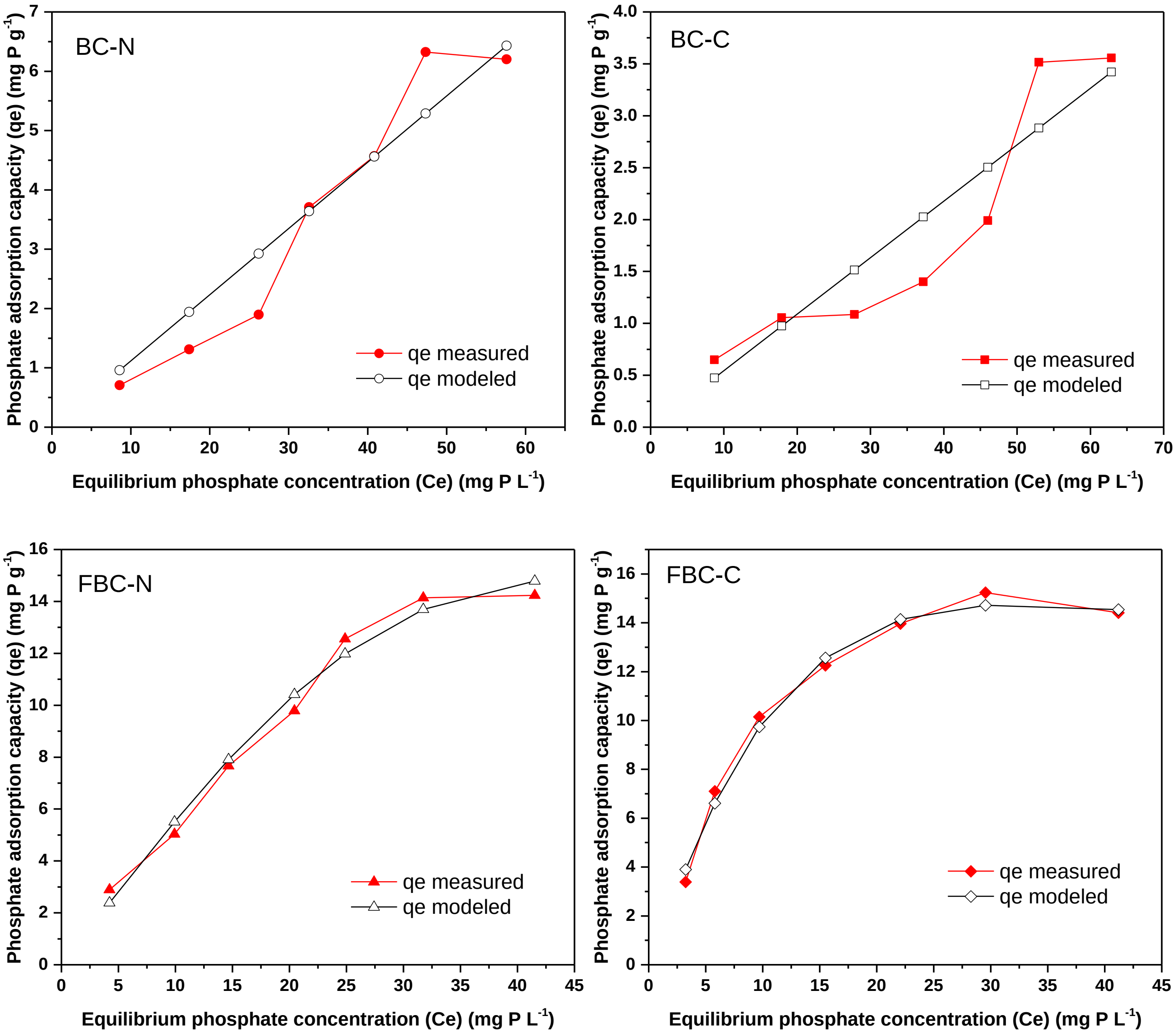

Fig. S6. Non-linear fitting of the Redlich-Peterson isotherm model for phosphate adsorption onto BC-N, BC-C, FBC-N, and FBC-C.

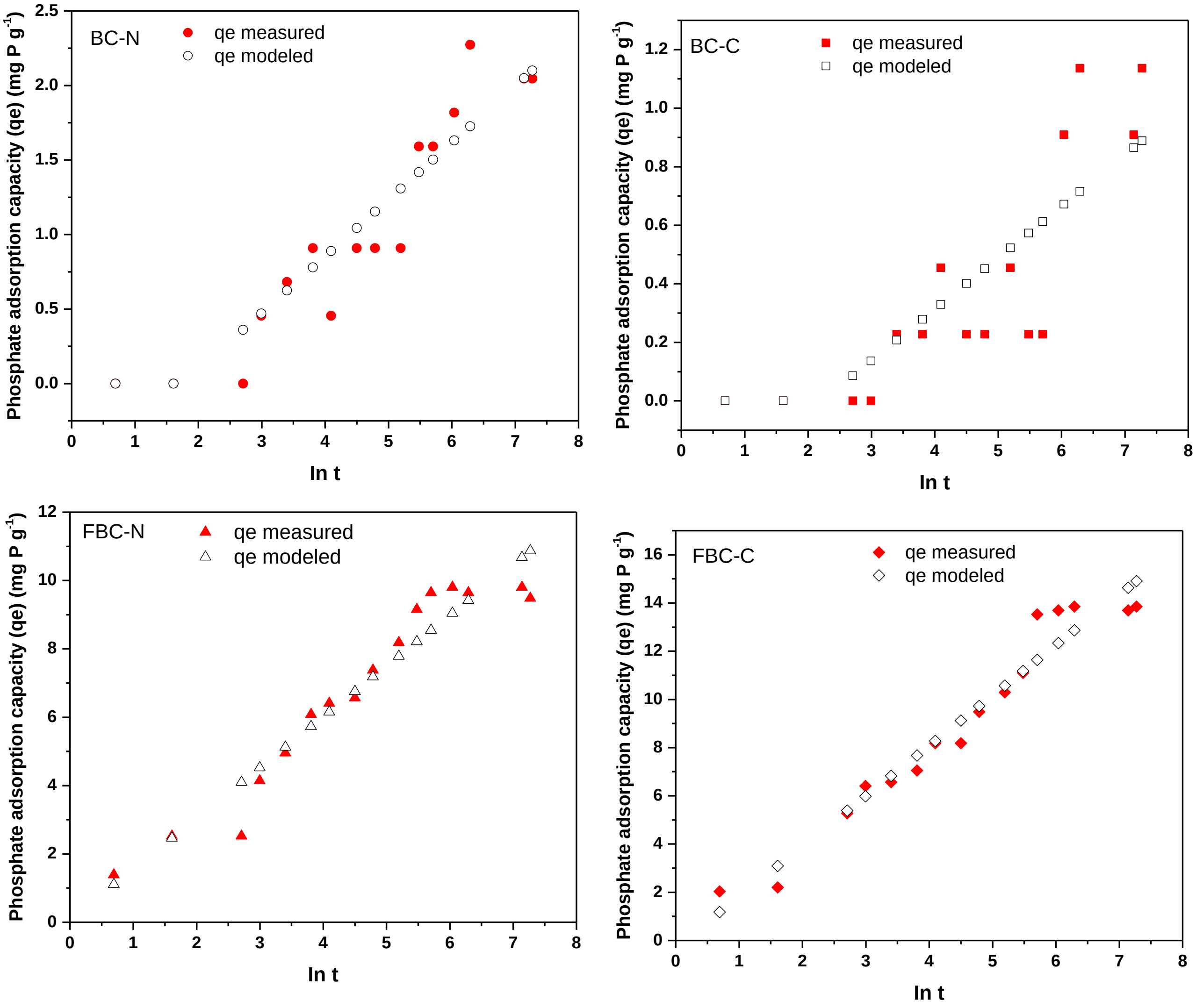

Fig. S7. Elovich model fitting of kinetic phosphate adsorption onto BC-N, BC-C, FBC-N, and FBC-C.

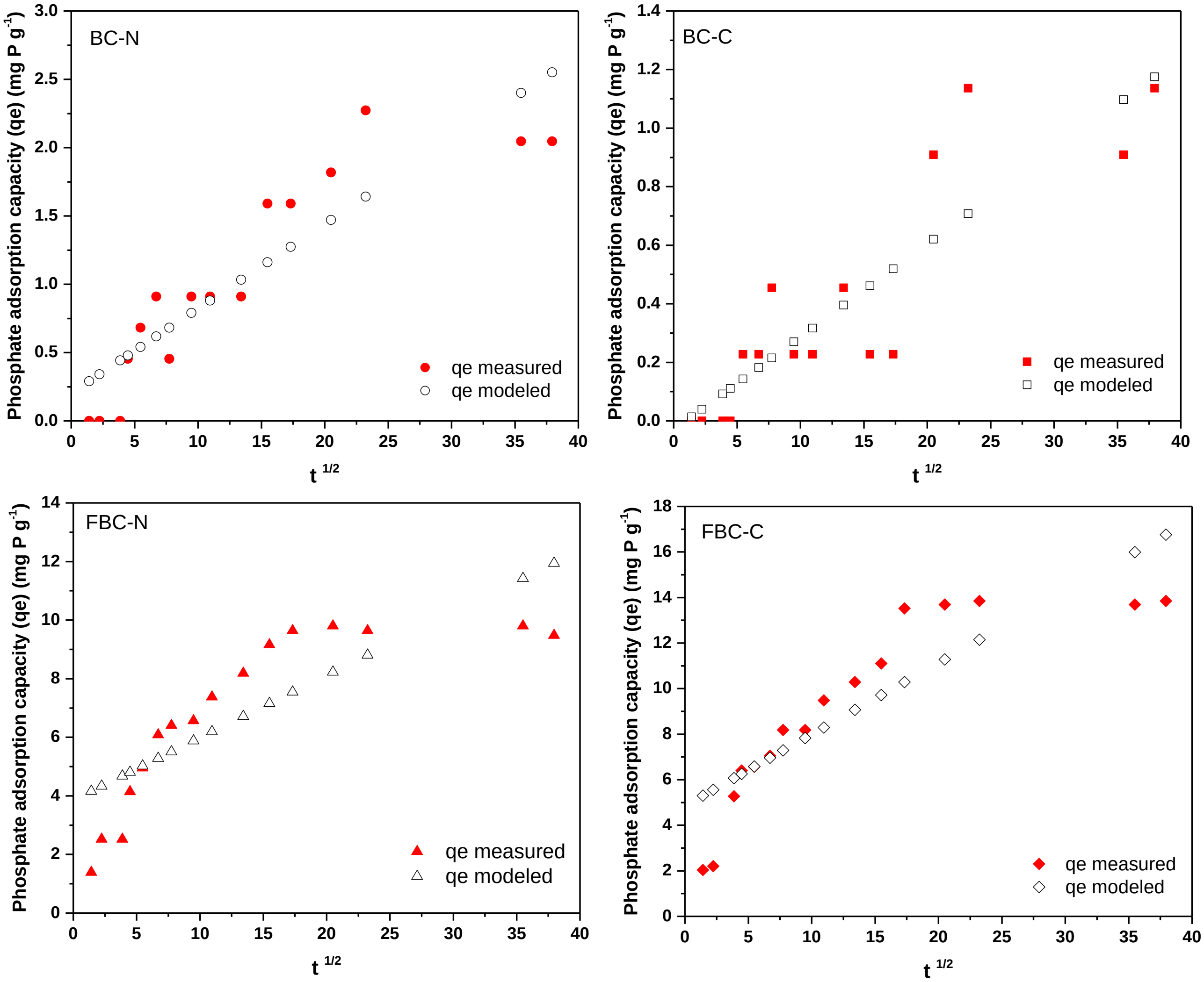

Fig. S8. Intraparticle diffusion model fitting of kinetic phosphate adsorption onto BC-N, BC-C, FBC-N, and FBC-C.

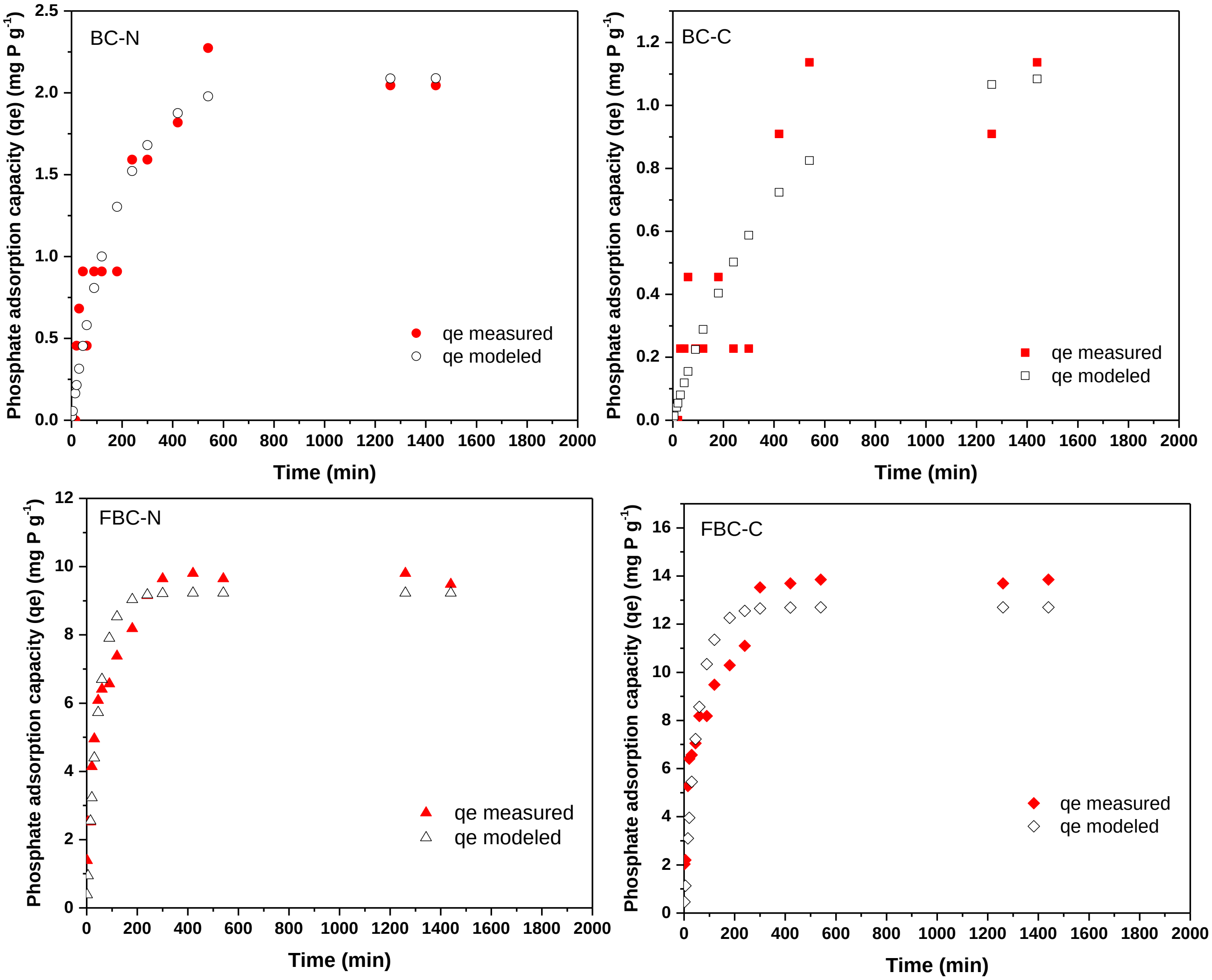

Fig. S9. Pseudo-first order model fitting of kinetic phosphate adsorption onto BC-N, BC-C, FBC-N, and FBC-C.

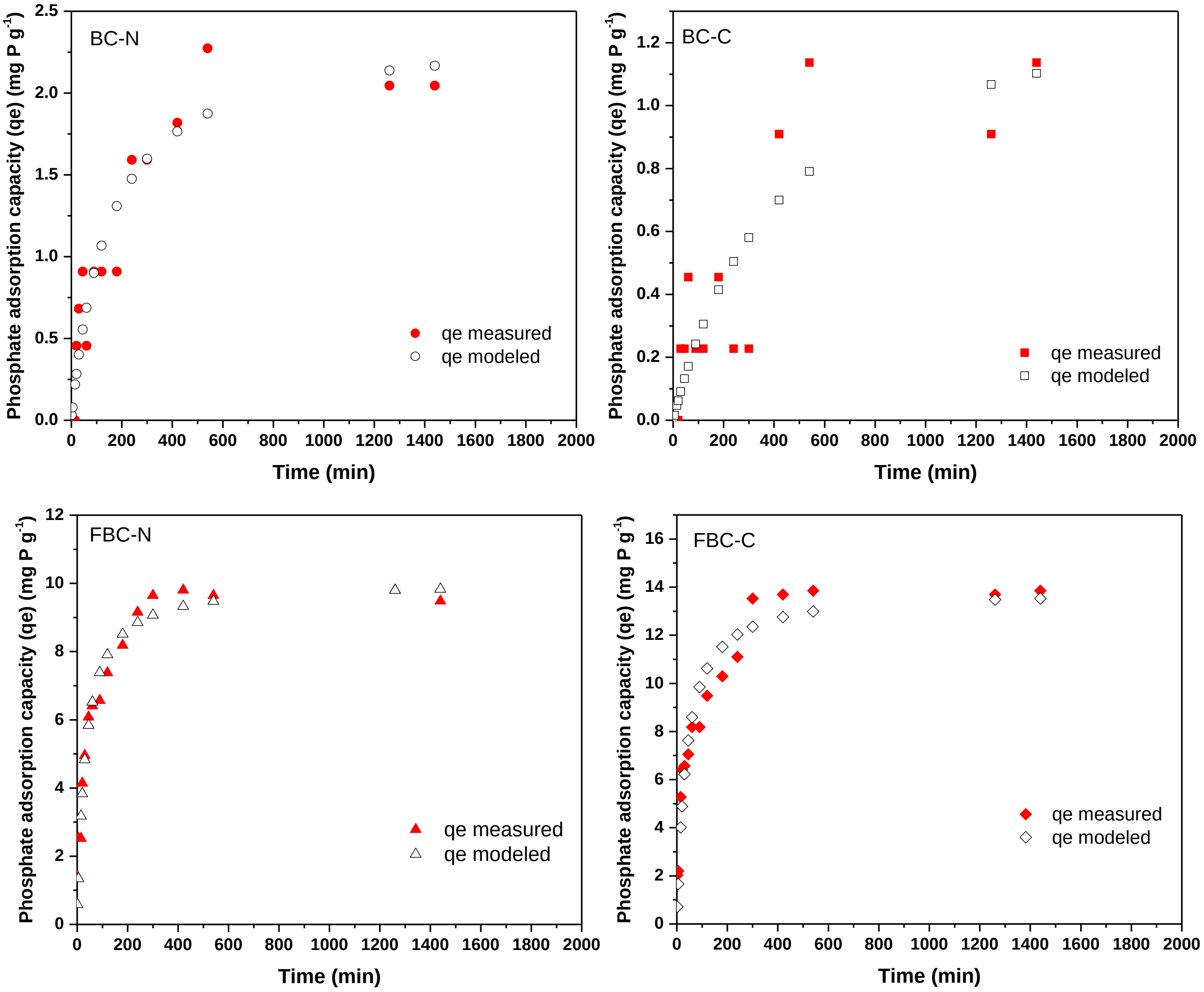

Fig. S10. Pseudo-second order model fitting of kinetic phosphate adsorption onto BC-N, BC-C, FBC-N, and FBC-C.

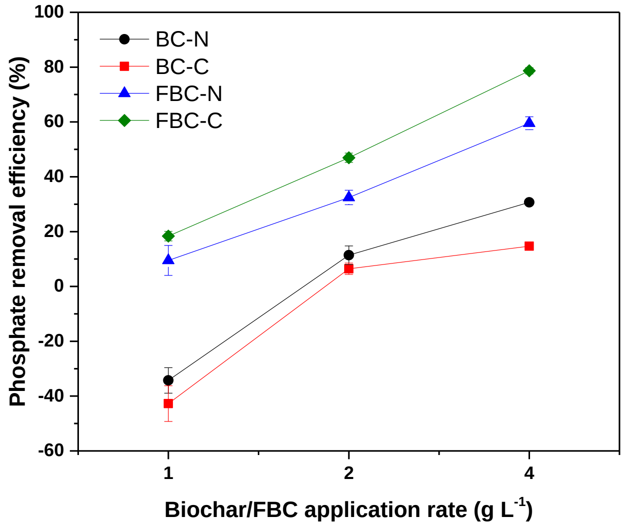

Fig. S11: Effect of adsorbent dosage on phosphate removal efficiency by BC-N, BC-C, FBC-N, and FBC-C.

References

Li, X., Hayashi, J., Li, C.Z. 2006. FT-Raman spectroscopic study of the evolution of char structure during the pyrolysis of a Victorian brown coal. *Fuel*, **85** (12-13), 1700-1707.

Lin-Vien, D., Colthup, N.B., Fateley, W.G., Grasselli, J.G. 1991. The handbook of infrared and Raman characteristic frequencies of organic molecules. Academic Press, San Diego, California, USA 477–490.

Nemanich, R., Glass, J., Lucovsky, G., Shroder, R. 1988. Raman scattering characterization of carbon bonding in diamond and diamondlike thin films. *Journal of Vacuum Science & Technology A*: **6**(3), 1783-1787.

Yang, X., Kwon, E.E., Dou, X., Zhang, M., Kim, K.-H., Tsang, D.C., Ok, Y.S. 2018. Fabrication of spherical biochar by a two-step thermal process from waste potato peel. *Science of the Total Environment*, **626**, 478-485.